VOLUME 9 | NUMBER 1 | 2025

DSIAC JOURNAL

MICRODIODE LASER PRIMERS – A PATH FORWARD

DSIAC JOURNAL

Volume 9 // Number 1 // 2025

Editor-in-Chief:
Aaron Hodges

Sr. Technical Editor:
Maria Brady

Graphic Designers:
Melissa Gestido, Katie Ogorzalek

The DSIAC Journal is a publication of the Defense Systems Information Analysis Center (DSIAC). DSIAC is a DoD Information Analysis Center (IAC) sponsored by the Defense Technical Information Center (DTIC) with policy oversight provided by the Office of the Under Secretary of Defense (OUSD) for Research and Engineering (R&E). DSIAC is operated by the SURVICE Engineering Company.

ISSN 2471-3392 (Print) // ISSN 2471-3406 (Online)

Distribution Statement A:
Approved for public release; distribution is unlimited.

On the Cover:
Digital Art Rendering *(Source: 123rf.com)*.

DSIAC Defense Systems Information Analysis Center

ABOUT DSIAC

Who We Are

A DoD Information Analysis Center comprised of scientists, engineers, researchers, analysts, and information specialists.

What We Do

Generate, collect, research, analyze, synthesize, and disseminate scientific and technical information (STI) to DoD and federal government users and industry contractors.

Why Our Services

To eliminate redundancy, foster collaboration, and stimulate innovation.

DSIAC SERVICES

Subject Matter Expert (SME) Connections

Access to a network of experts with expertise across our technical focus areas.

Technical Inquiries (TIs)

Up to 4 hours of FREE research using vast DoD information resources and our extensive network of SMEs.

Specialized Task Orders

Research and analysis services to solve our customer's toughest scientific and technical problems.

Webinars & Events

Our webinars feature a technical presentation from a SME in one of our focus areas. We also offer key technical conferences and forums for the science and technology community.

STI Collection

Our knowledge management team collects and uploads all pertinent STI into DTIC's Research & Engineering Gateway.

Information Research Products

The Defense Systems Digest, state-of-the-art reports, journals, TI response reports, and more available on our website.

CONTACT DSIAC

IAC Program Management Office

8725 John J. Kingman Road
Fort Belvoir, VA 22060
Office: 571.448.9753

DSIAC Headquarters

4695 Millennium Drive
Belcamp, MD 21017-1505
Office: 443.360.4600
Fax: 410.272.6763
Email: contact@dsiac.org

DSIAC Technical Project Lead

Taylor Knight
4695 Millennium Drive
Belcamp, MD 21017-1505
Office: 443.360.4600

FEATURED ARTICLE

MICRODIODE LASER PRIMERS - A PATH FORWARD

By Stephen Redington and Gregory Burke

Microdiode laser technology has a lot to offer across a span of multiple platforms. Low-cost, high-volume production is possible for military and commercial applications. There are many new applications that could be enabled by this technology, such as smart ammunition, nonenergetic tracers, time-delayed functions, and more. The technology also has the potential to solve manufacturing and reliability issues with current bridgewire technology that tends to be fragile in harsh environments. Perhaps the most appealing aspect of laser ignition is its ability to provide immunity from HERO on effects in the modern battlefield.

IN THIS ISSUE

ANALYSIS OF POWDER, BULLET, AND BARREL INTERACTIONS

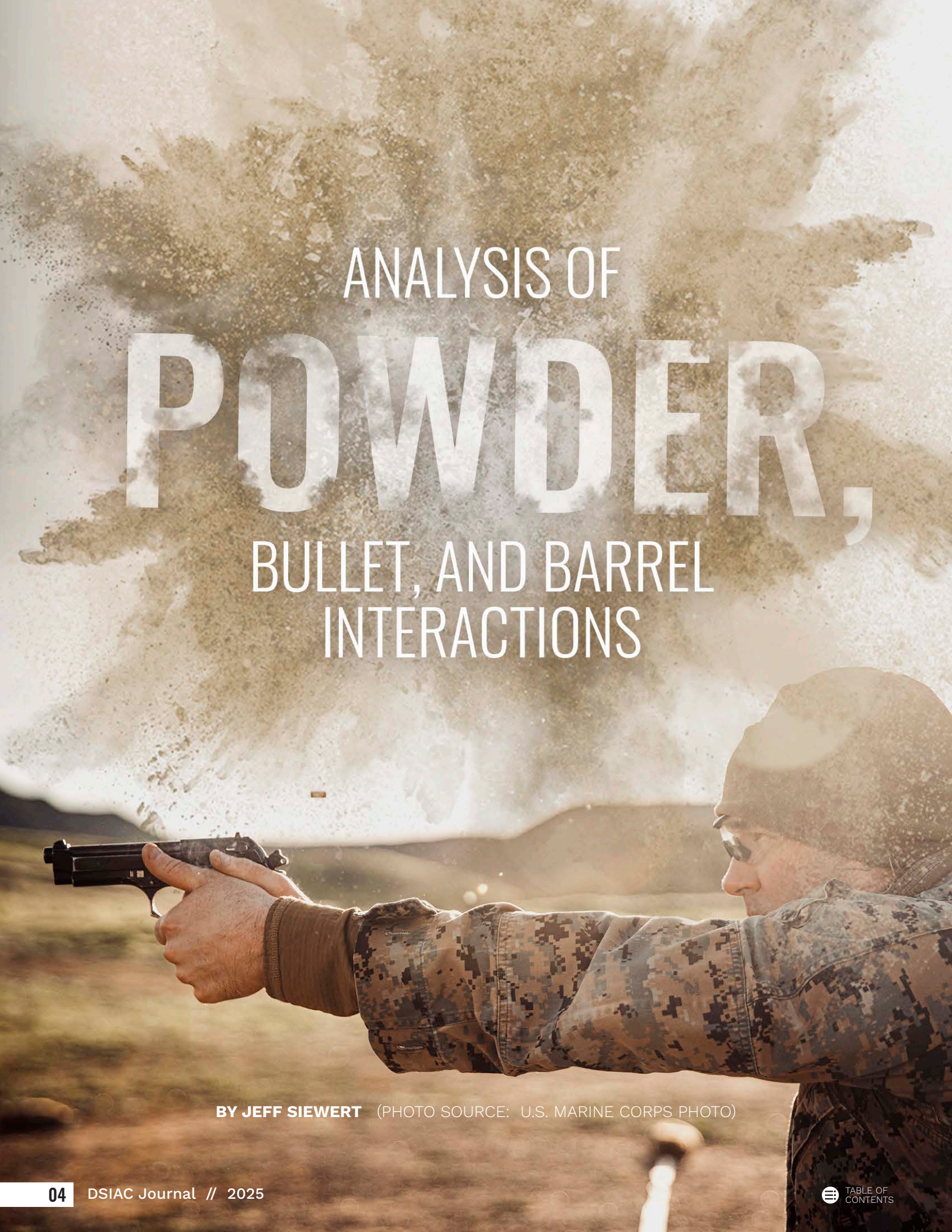

BY JEFF SIEWERT (PHOTO SOURCE: U.S. MARINE CORPS PHOTO)

INTRODUCTION

All ammunition makers and reloaders "know" that changing propellant type can affect the group size (dispersion) of the ammunition they make. Why changing powders affects bullet group size is more than a matter of propellant burnout prior to muzzle exit or some other easily definable characteristic. This article details the investigations undertaken to better understand this phenomenon and why it occurs.

BACKGROUND

Prior to this study, it was observed that powder simply provided the "push" for bullets if the propellant met the following conditions:

- Burned out prior to shot exit.
- Provided the desired muzzle velocity within the established pressure limits.
- Exhibited low muzzle velocity variation.

As a result of this study, it has been shown that propellant can also have a dramatic effect on group size.

Figure 1 shows the initial angle of attack (α) and the initial angular rate (ω) of the projectile at muzzle exit, exaggerated for clarity. The initial angular rate (ω) at muzzle exit is responsible for most of the short-range

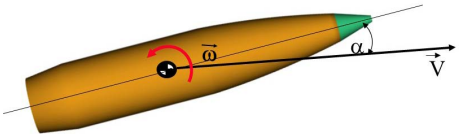

Figure 1. Initial Angle of Attack and Projectile Angular Rate *(Source: J. Siewert)*.

dispersion exhibited by small-caliber projectiles. The interaction between the flexible projectile and the flexible, nonstraight barrel bore is the source of the projectile's initial angular rate.

Variations in barrel pointing and translational velocity at muzzle exit also contribute to dispersion but generally to a much lesser extent.

A limited set of dispersion data was provided by Hornady Manufacturing Company on their 6.5-mm, 140-gr (extremely low drag - match [ELD-M]) projectiles using various propellant types. This projectile was selected because the manufacturer already had data and they were willing to share on this projectile. The powders used and analyzed were Varget, H4350, Hybrid H100-V, and W760, all distributed in the United States by Hodgdon [1]. The provided dispersion data was compared to the predicted dispersion data, and the findings were documented.

INTERIOR BALLISTICS

The first step was to ensure that the results from the Baer-Frankle lumped parameter, interior ballistics (IB) model used closely replicated, measured pressure-time history. To characterize propellants for use in this study, the predicted peak pressure and muzzle velocity were compared to published data from Hodgdon's annual reloading guide [1] for each powder. The data contained in their 2021 manual for the W760 simulations, along with Varget, H4350, and Hybrid H100-V, were used. Figure 2 shows a comparison

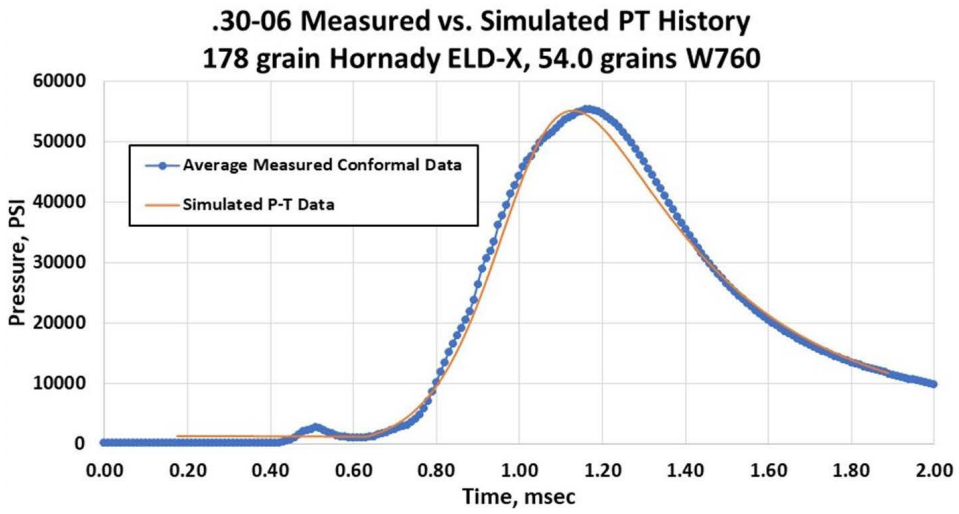

Figure 2. Comparison of Measured and Predicted Pressure-Time for the W760 Propellant *(Source: Hornady Manufacturing Company/J. Siewert)*.

between measured and predicted pressure-time history for 54.0 gr of W760 propellant in a .30-06 cartridge case firing 178-gr Hornady extremely low drag-expanding projectile.

For purposes of balloting simulations, it is important to match peak pressure and muzzle velocity, as well as the pressure rise rate; those parameters influence the structural dynamic behavior of the bullet-barrel combination. Qualitatively, the propellant model for the W760 propellant is in good agreement with measured data, as shown in Figure 2. Similar characterizations were performed for the other propellants examined.

Figure 3 shows the predicted average pressure-time histories for the studied propellants and respective charge weights. Statistical variations were generated for each powder based on the measured muzzle velocity standard deviation during firing.

Interior ballistics profiles were generated representing the average performance, along with plus and minus 1, 2, and 3 standard deviations from the mean. Figure 4 shows the mean performance for the 6.5-mm, 140-gr ELD-M when fired with 41.5 gr of H4350 propellant, along with the plus and minus 1, 2, and 3 standard deviations in muzzle velocity from the mean using a single resistance pressure vs. in-bore travel profile for all powders and variations.

Similar simulations were made for Varget, H100-V, and W760 to enable execution of balloting simulations with Monté Carlo draws for pressure-time forcing functions.

A summary of the propellant test characteristics used in this study is shown in Table 1.

PROJECTILE BALLOTING MODELS

The balloting simulation uses lumped mass and beam element models of the projectile and barrel to replicate the interaction of a flexible projectile in a flexible gun tube. In addition to the statistically variable pressure-time forcing functions, bore curvature

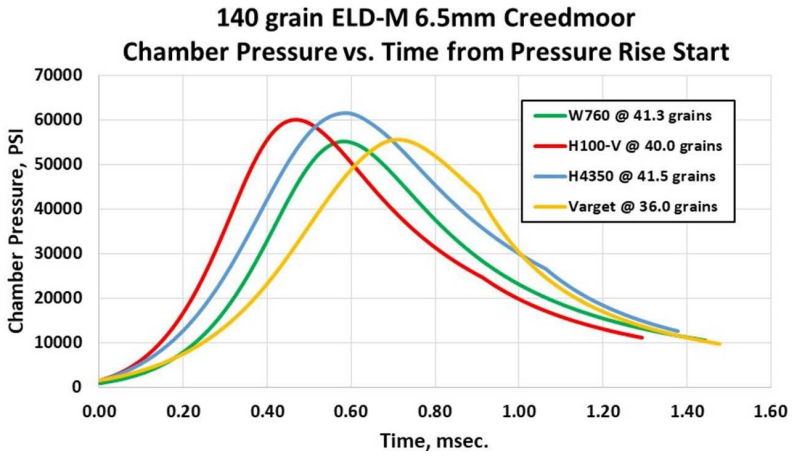

Figure 3. Comparison of Pressure-Time History for Studied Powders *(Source: J. Siewert)*.

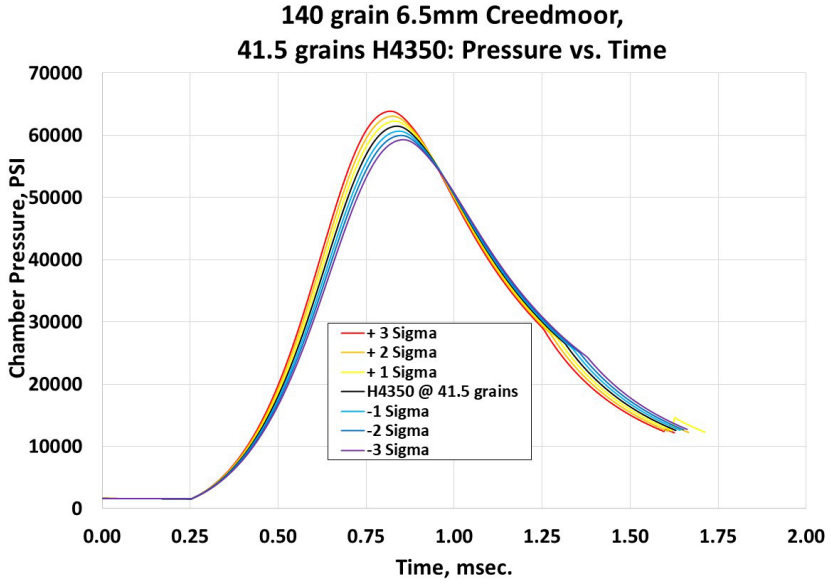

Figure 4. H350 Pressure vs. Time With Standard Deviations *(Source: J. Siewert)*.

Table 1. Summary of Propellant Test Performance *(Source: J. Siewert)*

PROPELLANT	CHARGE MASS (gr)	LOADING DENSITY (g/cm³)	MEAN MUZZLE VELOCITY (FPS)	MUZZLE VELOCITY SIGMA (FPS)	Pmax (PSI)
H4350	41.5	1.03	2781	8	59798
Varget	36.0	0.88	2654	4	55634
Hybrid H100-V	40.0	0.94	2704	10	60153
W760	41.3	0.98	2564	15	59080

Note: FPS = feet per second and PSI = pounds per square inch.

and variable initial conditions of the projectiles are input.

Figure 5 shows a comparison between the physical model of the 6.5-mm projectiles studied (top half of the images), along with the lumped mass and beam element model used by the balloting code and springs that support the projectile in the barrel as it accelerates along the tube (bottom half of the images). The studied projectiles are the 6.5-mm, 140-gr ELD-M and the 6.5-mm, 130-gr copper alloy expanding (CX) bullet.

The support springs connecting the projectile to the internal bore surface of the barrel are key to determining the dynamic response of the bullet to the longitudinal and lateral accelerations imposed on the structures by the firing event. For this study, values determined by finite-element analysis for similar projectiles were used. Table 2 shows the spring support stiffness values used for this study for the ELD-M and CX bullets.

Table 2. Stiffness Values for the 6.5-mm Bullet Bourrelets *(Source: J. Siewert)*

BULLET	BOURRELET	STIFFNESS (LB/IN)
140 g ELD-M	Rear	1,000,000
140 g ELD-M	Forward	1,000,000
130 g CX	Rear	2,000,000
130 g CX	Forward	2,000,000

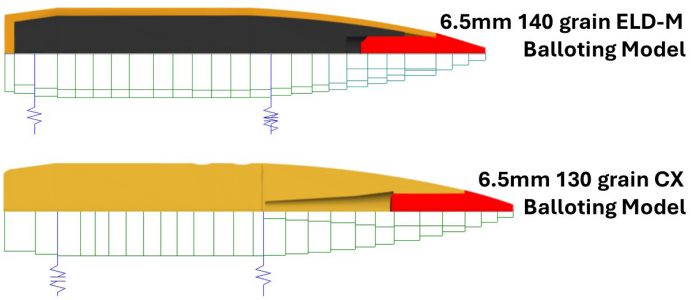

Figure 5. Comparison Between the 6.5-mm Bullets Physical and Balloting Models *(Source: J. Siewert)*.

BARREL BALLOTING MODELS

The balloting simulation also requires lumped mass and beam element models for the barrels being assessed. Figure 6 shows the 6.5-mm physical model (above the horizontal centerline) and the lumped mass and beam element model used by the balloting simulation for the "tapered barrel" assessments.

Figure 7 shows the 6.5-mm physical model (above the horizontal centerline) and the lumped mass and beam element model used by the balloting simulation for the "heavy barrel" assessments.

For several of these analyses, the support springs were moved from the aft (chamber) end of the barrel to a mid-barrel location to assess the effect of moving the barrel clamping location on the resulting projectile exit state's (angular rate and cross velocity) distribution and concomitant dispersion. The "statistical" simulation runs 500 iterations performing a Monté Carlo draw on the projectile's initial position and IB's forcing function; but for these analyses, the simulations were run twice to obtain 1,000 replications per unique set of interface and boundary conditions.

Another important input to the balloting simulation is the bore centerline profile (bore straightness).

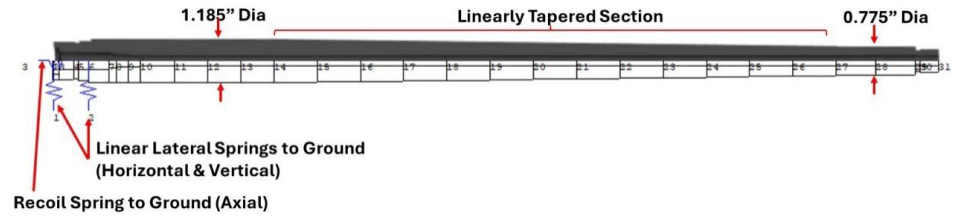

Figure 6. "Tapered" Barrel Physical and Balloting Models *(Source: J. Siewert).*

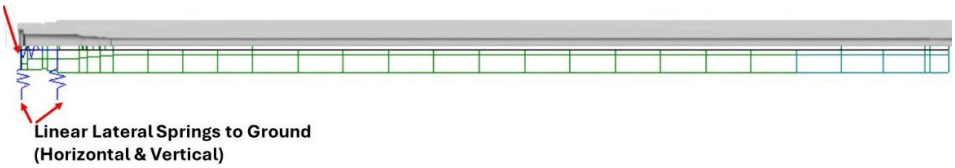

Figure 7. "Heavy" Barrel Physical and Balloting Models *(Source: J. Siewert).*

Figure 8 shows the two vertical bore centerline profiles—"benign" and "moderate" bores. The bores are straight in the horizontal plane.

PROJECTILE INITIAL CONDITIONS

The last important input set for the balloting simulations is the initial conditions for the projectile(s). The two primary input categories that determine the projectile's initial position are the bourrelet diameter (mean and standard deviations) and the establishment of the projectile's initial plane of motion. These inputs are shown in Figure 9 with the blue and red arrows, respectively.

Two general sets of initial plane-of-orientation conditions were explored—the first being a limited set of pointing angles and the second being an unlimited set of pointing angles. For guns with a spring-loaded ejection plunger, the force applied to the base of the cartridge case by the plunger was thought to result in a preferred initial pointing orientation ("around-the-clock" as viewed from the breech) of the bullet as it was placed into the barrel.

> ***The last important input set for the balloting simulations is the initial conditions for the projectile(s).***

The "uniform" distribution was subsequently determined to be preferred, as the limited set of pointing angles typically resulted in a "skewed" fall of shot distribution (horizontal vs. vertical axis larger or vice versa), which was inconsistent with typical observed circular dispersion patterns.

SIMULATION RESULTS

Initial propellant-bullet-barrel simulations were made in the benign, tapered barrel. A plot was made of the bullet exit states, initial angular rate, and initial cross velocity magnitudes as a function of standard deviation from the mean for each propellant. This yielded some very interesting "exit state response maps" for the 140-gr, 6.5-mm projectile. Plots for

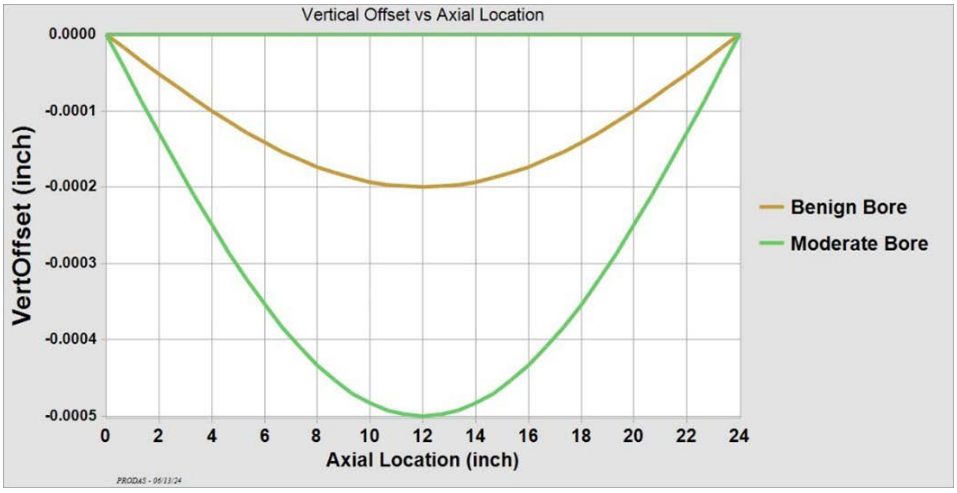

Figure 8. Bore Centerline Deviation vs. In-Bore Travel (Axial Location) *(Source: J. Siewert).*

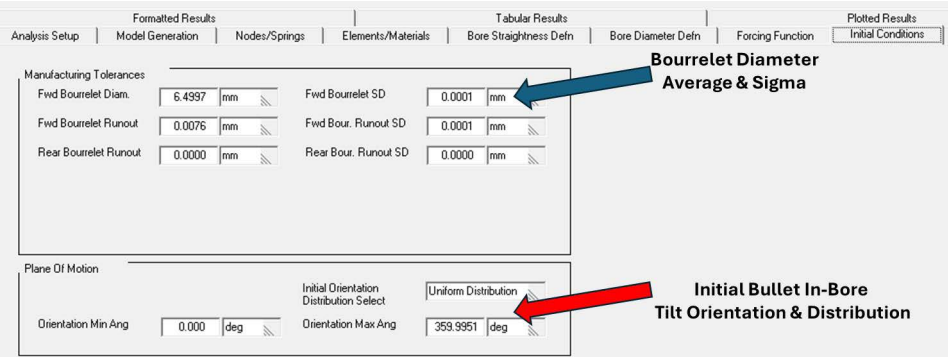

Figure 9. Initial Conditions Input for the 6.5-mm Bullet *(Source: J. Siewert)*.

each of the propellants are shown in Figure 10. The differences among all the propellants are interesting, and the impact point for an individual shot is the result of a paired set of exit state angular rate and cross velocity at a given distance from the mean for a particular randomly selected, IB forcing function.

As seen in Figure 10, all the initial yaw rate plots exhibit significant "waves" in their response to changes in pressure-time history; some zones of pressure-time performance are much more likely to result in larger initial yaw rates, and some velocity zones are far less likely to exhibit high exit rates. The same can be said for the cross-velocity behavior but to a much lesser extent.

Of particular interest in Figure 10 is the exit yaw rate response of the Hybrid H100-V, shown in the upper right corner between 0 and +1 standard deviation from the mean. Here, the structural response is "bifurcated," with some shots exhibiting relatively large yaw rates and others exhibiting small yaw rates, with nearly nothing in between. For this propellant-bullet-barrel combination in the region between the mean and plus-one standard deviation above the mean, ~1/3 of shots exit with an angular rate above 10 rad/s, while 2/3 are below that figure, all while exhibiting a narrow band of cross-velocity response. This response anomaly was intriguing and studied further, as discussed next.

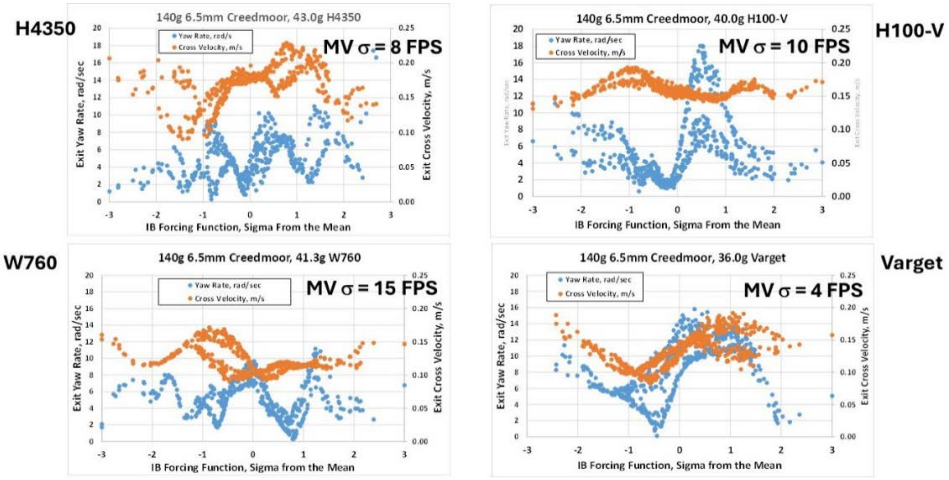

Figure 10. ELD-M Exit States vs. Propellant Type in a Benign, Tapered Barrel for the 140-gr, 6.5-mm Projectile *(Source: J. Siewert)*.

Based upon Bob McCoy's "Modern Exterior Ballistics: The Launch and Flight Dynamics of Symmetric Projectiles" [2], the aerodynamic "jump" from the initial angular rate is in a direction that tends to cancel the "throw" arising from the bullet cross velocity at muzzle exit, provided the cross velocity is caused only by the center of gravity (CG) offset of a "perfectly made" bullet that is tipped in-bore relative to the bore centerline at muzzle exit. In this case, the exit angular rate and cross velocity should be well correlated, with a correlation coefficient of 0.75 or greater. An examination of the exit states captured from this analysis shows the correlation coefficient of all the propellants studied under any set of boundary conditions was no greater than 0.45. This means that the cross velocity of the propellant-bullet-barrel combinations studied most likely arises from the combined effects of barrel pointing and transverse motion and not the product of CG offset multiplied by the exit spin rate.

It should be noted that the velocity "period" of the structural dynamic response changes is on the order of one or two velocity standard deviations, meaning that the (re)loader does not have any chance to "tune" the muzzle velocity to a point where the large exit yaw rates do not occur. The effect of changing average muzzle velocity on the structural response for the Hybrid H100-V is shown in Figure 11, along with several other changes in the "system" parameters.

Since the exit yaw rate structural response "map" of the Hybrid H100-V propellant was so interesting between the mean performance and plus-one standard deviation, bullet-barrel interface parameters that could be changed to modify the response in that region were explored. Figure 11 shows the "baseline" simulation response (tapered, benign barrel with limited initial projectile tilt plane angles shown in the upper left), along with the response with a barrel with a straight outside diameter in the upper right. Unsurprisingly, a reduction in both angular rate and cross velocity is seen since this change increases the bending stiffness of the barrel and its mass.

The structural response with the same benign, tapered barrel with limited start planes is seen in the lower left-hand corner of Figure 11. However, the average muzzle velocity has been reduced by 20 FPS, along with all the

> ***The cross velocity of the propellant-bullet-barrel combinations studied most likely arises from the combined effects of barrel pointing and transverse motion.***

velocity standard deviations. This value was chosen because if the exit state structural response related solely to the average muzzle velocity, a 20 FPS shift in velocity should have moved the bifurcated response to the plus 2–3 sigma range if the behavior was linearly sensitive to muzzle velocity alone. Interestingly, while there is a reduction in angular rate between the mean and plus-one standard deviation, there is still a bifurcation in the yaw rate response in that region with the chosen set of initial conditions and the bore straightness profile.

Subsequently, the initial conditions were changed from limited start plane angles to unlimited, meaning the axis of the bullet can randomly point anywhere "around the clock" as viewed from the chamber when the cartridge is seated. With this set of initial conditions for the projectile, the angular rate "bifurcation" between the mean peak pressure and plus-one standard deviation essentially disappeared and was replaced by a broader, reduced angular rate response.

Next, the bullet exit state response was evaluated for the tapered, benign barrel, with the connection between the barrel and "ground" changed from the aft end of the barrel at the chamber to the middle of the barrel. The structural response maps for this analysis are shown in Figure 12. The supports at the aft end are shown on the left-hand side of the figure, while

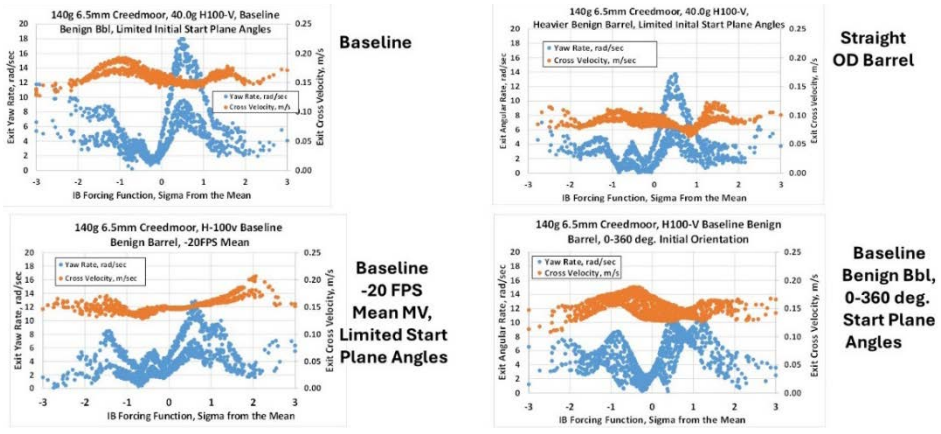

Figure 11. ELD-M Exit States vs. Various Interface Perturbations for the 140-gr, 6.5-mm Projectile *(Source: J. Siewert)*.

the response for the system with the barrel supports located at the mid-barrel location is shown on the right. There is a clear reduction in exit angular rate and cross velocity with the mid-barrel support location. This clearly supports the decision of the manufacturers to connect the barrels to their slide block assemblies' mid-barrel as the "low dispersion" choice.

From there, the exit state structural response caused by arbitrarily changing the support stiffness of the projectile was evaluated. This is an academic exercise in that the support stiffness of the bullet is determined primarily by the bullet construction and materials. While the bullet support stiffness can be reduced some using cannelures, the reduction in bourrelet stiffness to 750,000 lb/in is exceptionally small given the bullet construction.

Figure 13 shows the exit state response map for the 6.5-mm, 140-gr ELD-M projectile, with 1.5 million lb/in support stiffness on the left and 750,000 lb/in stiffness on the right. There is a clear reduction in both exit yaw rate and cross velocity, with reduced support stiffness. This result runs contrary to the general experience of medium- and large-caliber ammunition.

Lastly, curiosity about the exit state response map and expected dispersion of the 140-gr, 6.5-mm ELD-M compared to the monolithic copper alloy 130-gr, 6.5-mm CX projectile for the two bore centerline profiles analyzed prompted comparative investigations about these two bullets. Figure 14 shows the exit state structural response maps of the ELD-M projectile on the left, with the CX projectile response on the right. The exit state response of the bullets to the barrel with a 0.0002-in maximum bore centerline deviation is on the top, while the maps for the same bullets and initial conditions with 0.0005-in maximum bore centerline deviation are on the bottom.

It is clear in Figure 14 that the exit yaw rate and cross velocity of the

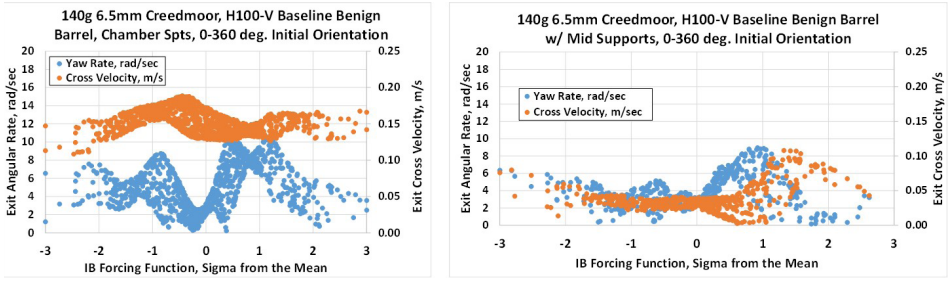

Figure 12. ELD-M Exit States vs. Barrel Support Location for the 140-gr, 6.5-mm Projectile *(Source: J. Siewert)*.

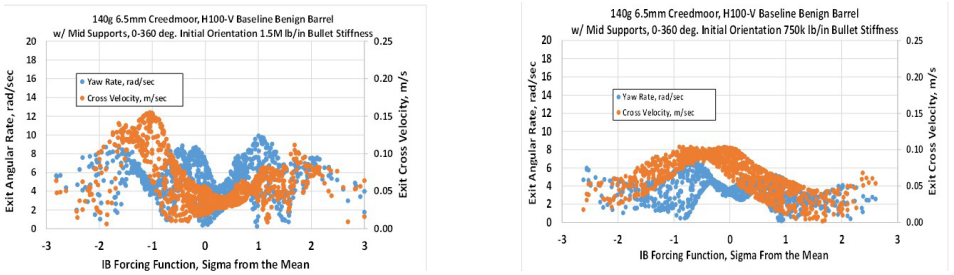

Figure 13. ELD-M Exit States vs. Bullet-Barrel Support Stiffness for the 140-gr, 6.5-mm Projectile *(Source: J. Siewert)*.

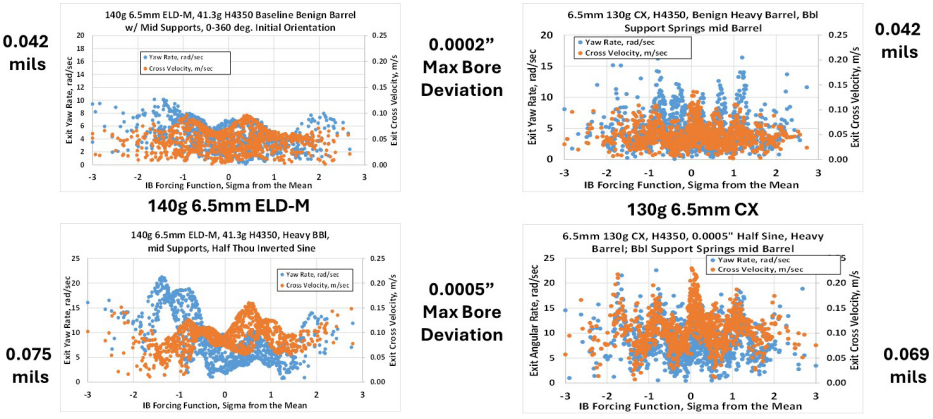

Figure 14. ELD-M and 130-gr CX Exit States vs. Max Bore Deviation for the 140-gr, 6.5-mm Projectile *(Source: J. Siewert)*.

CX bullet are more sensitive to changes in pressure-time history than the ELD-M, but the dispersion performance appears to be comparable with an identical bore shape. Because these results are for the analyzed bore centerlines that are half-sine waves, the comparative dispersion performance of these bullets may be considerably different in barrels with different bore centerline shapes. The cleanliness of the barrel will play a significant role in the observed dispersion.

Table 3 lists the interior ballistics simulation and dispersion simulation performance of the 6.5-mm, 140-gr ELD-M projectile vs. the various propellants examined.

> ***The cleanliness of the barrel will play a significant role in the observed dispersion.***

As shown in the last row of Table 3, there is generally poor correlation between the bullet exit states and the interior ballistics performance. This means that the extremes in pressure-time performance are NOT responsible for the large angular rate and/or large cross velocity that cause the "fliers" that plague all shooters.

How do the results of the balloting simulation compare to the dispersion seen during testing? Figure 15 shows the dispersion seen in product testing vs. propellant type and the dispersion predicted by the balloting code.

As seen in the figure, the dispersion predicted by the balloting code of the 6.5-mm, 140-gr ELD-M using the two extruded powders, H4350 and Varget, is in close agreement with the dispersion observed in test, while the

Table 3. ELD-M – Propellant Characteristic Performance Summary for the 140-gr, 6.5-mm Projectile *(Source: J. Siewert)*

CHARACTERISTIC	UNITS	H4350	VARGET	HYBRID 100-V	W760
Maxium charge weight	gr	41.5	36	40	41.3
Pmax simulation	PSI	59798	55634	60153.82	59080
MV measured	FPS	2781	2644	2704	2564
MV simulation	FPS	2781	2654	2704	2564
MV slope simulation	FPS/gr	63.00	61.75	48.00	50.00
MV sigma data	FPS	8	4	10	15
Base press at exit	PSI	10543	8401	10035	10651
Maximum acceleration	"G's"	131137	145106	131889	126572
10%–90% rise time	ms	0.350	0.441	0.292	0.334
Powder burnout	% of max travel	0.568	0.295	0.993	1.00+
95% group size	in/200 yd	1.91	1.23	3.22	2.006
Balloting simulation dispersion	mils	0.086	0.054	0.042	0.028
Angular rate average	rad/s	4.949	8.462	5.863	5.175
Angular rate sigma	rad/s	2.283	3.608	4.001	2.162
X velocity average	m/s	0.17	0.13	0.16	0.12
X velocity sigma	m/s	0.03	0.03	0.01	0.02
Exit rate and X velocity correlation from balloting	—	0.44	0.36	0.17	–0.11

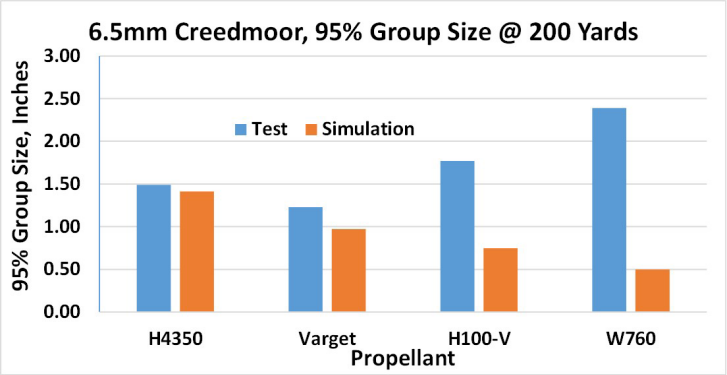

Figure 15. ELD-M Measured vs. Simulated Dispersion for the 140-gr, 6.5-mm Projectile *(Source: Hornady Manufacturing Company/J. Siewert).*

H100-V and W760 results do not agree well at all. Years of experience with the balloting code has shown if the predicted dispersion is radically different from that observed in test, the most likely cause is something the balloting code does not consider, like a disturbance from reverse flow at muzzle exit. The H100-V and W760 are hybrid and ball powders, respectively, and the interior ballistic simulations indicate these powders may not be completely consumed at muzzle exit. Unburned propellant grains striking the aft end of the projectile at shot exit (along with accompanying high base pressures at exit) are the most likely explanation for this discrepancy.

Externally applied loads can cause significant additional dispersion if the load is applied in the "wrong" place. From previous studies on the dispersion of spin-stabilized bullets, if a fixed impulse is applied perpendicular to the longitudinal axis of a projectile for one-half revolution, the angle of attack and trajectory "jump" angle that result are shown in Figure 16. The minimum angle of attack developed by the projectile is seen when applied impulse is located at the projectile's center of mass, while the minimum trajectory deviation (the "jump angle") is minimized when applied perpendicular to the projectile's normal force center of pressure location. Also shown is that the trajectory deviation is maximized when the impulse is applied at the aft end of the projectile, farthest from the normal force center of pressure.

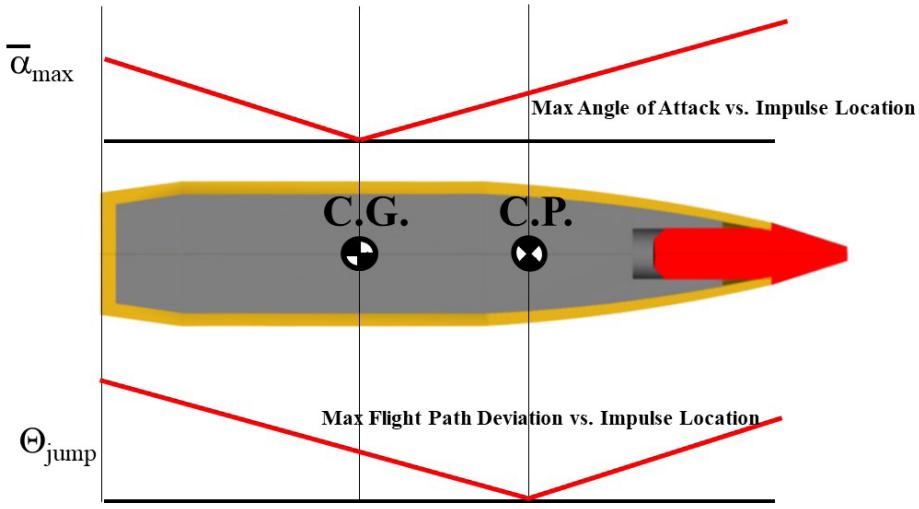

Figure 16. Projectile Max Angle of Attack and Flight Path Deviation as a Function of Perpendicularly Externally Applied Impulse Location Along the Projectile Body *(Source: J. Siewert).*

If the base pressure at muzzle exit is excessively high and randomly asymmetric or unburned propellant grains strike the projectile at the bullet base, the dispersion of the projectile can be adversely affected.

CONCLUSIONS

Each combination of propellant, bullet, and barrel (geometry, support stiffness and location, twist rate, etc.) exhibits a unique "exit state structural response" due to the system structural response to the differing rise rates of the propellants used. These results conclusively show that propellant selection can indeed affect dispersion. Choosing a powder that burns out prior to muzzle exit will likely help keep groups small.

In viewing the various response maps, it is easy to see how a reloader could

think a dispersion "node" had been found when shooting 3, 5, or 10 shot sample sizes. Propellant screening testing should thus be viewed as a "go/no-go" exercise for bullet-powder compatibility. ■

ACKNOWLEDGMENTS

The author would like to thank the following companies:

- Arrow Tech Associates, Inc. [3] for the continued use of their analytical software.
- Hornady Manufacturing Company for their gracious sharing of test data.

REFERENCES

[1] Outdoor Sportsman Group. *Hodgdon Reloading Manual*. New York, NY, 2021.

[2] McCoy, R. L. "Modern Exterior Ballistics: The Launch and Flight Dynamics of Symmetric Projectiles." Atglen, PA: Schiffer Publishing, Ltd., 1 January 2004.

[3] Arrow Tech Associates, Inc. PRODAS software, www.prodas.com, 1998–2023.

BIOGRAPHY

JEFF SIEWERT is a retired ballistics engineer who has conducted studies on bullets, propellants, cartridge cases, trajectory matches, radar data reduction, bullet-barrel interactions (in-bore balloting and body engraving simulations), and rifling design in calibers ranging from 17 cal to 203 mm. His studies on small-caliber projectiles have included dispersion reduction on the M855A1 and M856A1; balloting and dispersion analyses for the next generation squad weapon, general purpose projectile; engraving force measurements on military and commercial bullets and studies on barrel configuration and dispersion; and case-chamber interaction studies to troubleshoot case failures. He is the 2024 recipient of the National Defense Industrial Association's Chinn Award. Mr. Siewert holds a B.A. in physics from State University of New York at Oswego.

PERCEPTION AND NAVIGATION ALGORITHMS FOR LEGGED ROBOTS

BY ADARSH JAGAN SATHYAMOORTHY, KASUN WEERAKOON, MOHAMED ELNOOR, JASON PUSEY, AND DINESH MANOCHA (PHOTO SOURCE: SHUTTERSTOCK)

INTRODUCTION

Mobile robots, equipped with wheels, tracks, or legs, are designed to move from a start location to a goal in various indoor and outdoor environments. A key area of interest is making them capable of autonomously navigating diverse environments.

Within mobile robots, legged robots have been used for many applications in outdoor settings like surveillance [1], inspection in power plants and factories [2], reconnaissance [3], disaster response [4], and planetary exploration [5] due to their superior dynamics, which enables them to traverse challenging outdoor terrains [6, 7]. For these applications, a robot may have to first perceive various terrains and their challenges, different kinds of obstacles (e.g., rocks, trees, tall grass, ditches, etc.), and dimensions and properties (hardness, pliability/bendability, overhanging objects, etc.). Next, it must make navigation decisions to either avoid nontraversable terrains and obstacles or use locomotion strategies to traverse them stably. Three components—perception (what terrains and obstacles are nearby), navigation (where the robot must walk), and locomotion (how the robot must walk)—form the core of legged robot autonomy.

Legged robots perceive their environments through two possible ways—exteroception and proprioception. Exteroception refers to sensing the environment using visual sensors such as red, green, and blue (RGB)/RGB-depth (RGB-D) cameras, two-dimensional (2-D) or three-dimensional (3-D) light detection and ranging (LiDAR) methods, radars, etc. Conversely, proprioception refers to sensing the environment using the robot's internal states such as leg joint positions, velocities, joint forces, torques, etc. The robot's navigation or planner, on the other hand, computes trajectories or velocities for the robot to execute based on the perceived environment complexities.

The work presented in this article deals with local planning, i.e., computing trajectories over a short time horizon based on local sensing (~ tens of meters). The robot's locomotion computes its leg poses and contact points on the ground for stable traversal on any terrain or object that the robot can climb over. Given these components, the challenges to legged robot autonomy in unstructured outdoor terrains are discussed in the next section.

> ***Three components—perception, navigation, and locomotion—form the core of legged robot autonomy.***

CHALLENGES IN UNSTRUCTURED OUTDOOR NAVIGATION

Unstructured, off-road terrains are characterized by a lack of predefined pathways; uneven terrains; the presence of random natural obstacles like rocks, fallen branches, various vegetation (trees of various sizes, bushes, tall grass, reeds, etc.); and negative obstacles like pits and ditches. The challenges created by these characteristics are briefly discussed next.

Terrain

In unstructured terrains, the robot's legs could slip, trip, sink, or get entangled in vegetation. Therefore, a robot could crash due to one of the following reasons:

- Poor foothold: This causes the robot's feet to slip in rocky or slippery terrains like ice because the surface does not provide enough grip or traction for the robot to stand or walk.
- Granularity: This causes the robot's feet to sink into the terrain (e.g., sand, mud, and snow), leading to incorrect measurements of joint states. This could cause the robot's locomotion controller to overcompensate to stabilize itself, resulting in crashes.

- Resistance to motion: This is typically caused by dense, pliable vegetation (PV) that can be walked through (e.g., tall grass and bushes) but requires significantly higher effort (motor torques) from the robot to traverse. Additionally, the robot's legs could get entangled in vegetation, resulting in a crash.

Dense Vegetation

In unstructured outdoor settings, a major challenge arises from different kinds of vegetation. Vegetation can be fundamentally classified into one of the following categories: (1) tall grass of variable density, which is pliable (therefore, the robot can walk through) and could be taller than the robot's sensor-mounting height, causing occlusions; (2) bushes/shrubs that are typically dense and shorter than the robot and detectable without occlusions; and (3) trees (>2 mm high), which are nonpliable/untraversable and must be avoided.

Navigating through such vegetation, the robot could encounter the following adverse phenomena:

- Freezing: The robot's planner proclaims that no feasible trajectories or velocities exist to move toward its goal and halts it for extended time periods.
- Entrapment: The commanded velocity by the planner is non-zero, but the robot's actual velocity is near-zero due to its legs getting stuck in vegetation or other entities.
- Collisions: The robot does not detect a nonpliable obstacle like a bush or tree and collides with it.

Vegetation also poses a major challenge to exteroception due to occlusions and the lack of clear boundaries between different kinds of vegetation. For instance, tall grass could be occluding trees, leading to erroneous detections and collisions.

More complex challenges and potential methods to address them are discussed in the "Future Work" section.

PROPOSED SOLUTIONS

In this section, some proposed perception and navigation algorithms addressing these challenges are discussed.

Perceiving Uneven, Granular Terrains

To address terrain challenges, the robot must first accurately estimate their traversability. Traditional navigation methods relying solely on exteroceptive sensing (e.g., cameras and LiDARs) or proprioceptive feedback (e.g., joint encoders) often fall short in complex terrains or when environmental conditions (e.g., adverse lighting) affect sensor reliability. Therefore, closely coupling exteroceptive and proprioceptive sensing and adaptively utilizing the more reliable mode of sensing for estimating terrain traversability at any instant are proposed.

To this end, Adaptive Multimodal Coupling (AMCO) [8], a novel method that utilizes three distinct cost maps derived from the robot's sensory data, is suggested. The three maps are (1) the general knowledge map, (2) the traversability history map, and (3) the current proprioception map. These maps combine to form a coupled traversability cost map (shown in Figure 1), which guides the robot in selecting stabilizing gaits and velocities in terrains with poor footholds, granularity, and resistance to motion. In the figure, the input image is passed through a segmentation model to segment the image into different terrain types (left). Then, the AMCO utilizes proprioception and segmented images (center) to generate a couple traversability cost map C_{amco} (right). AMCO's main components are described next.

General Knowledge Map

The general knowledge map represents a terrain's general level of traversability (e.g., walking on soil is generally stable). It is generated using semantic segmentation of RGB images [9] to classify terrain types and their expected traversabilities. The segmentation process categorizes each pixel into predefined classes (e.g., stable, granular, poor foothold, and high-resistance terrains). This map assigns traversability costs based on these classifications utilizing a model that incorporates the smallest area ellipse derived from principal component analysis of terrain data

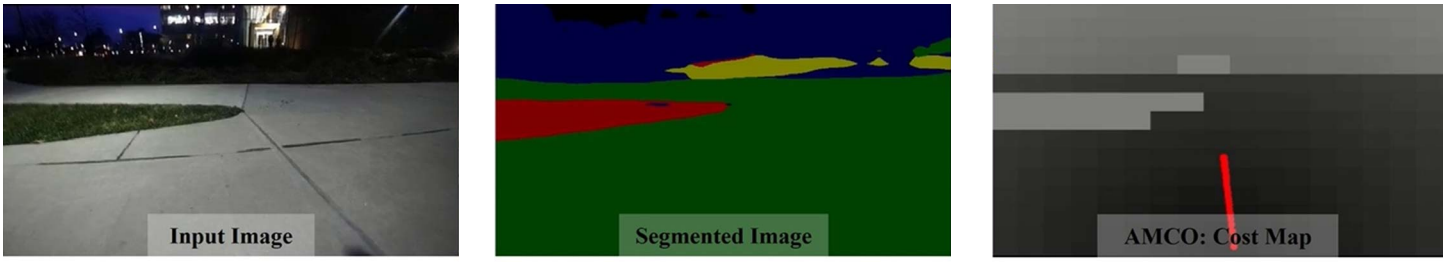

Figure 1. Traversability Cost Map Generation Using AMCO [8], Where Light Colors Indicate High Costs and Vice Versa *(Source: M. Elnoor)*.

[10]. This process involves discretizing the segmented image into grids and assigning costs based on the predominant terrain type within each grid (see Figure 1 [right]).

Traversability History Map

The traversability history map reflects changes in terrain conditions that might not be immediately apparent from visual data (e.g., soil felt wet and deformable a few times in another location). It records the robot's recent experiences on a terrain as proprioceptive signals for a certain duration and adjusts the costs in the general knowledge map dynamically based on the new information. This approach ensures that recent, context-specific data inform the robot's navigation strategy, improving its adaptability to changing terrain conditions.

Current Proprioception Map

The current proprioception map provides a real-time assessment of the terrain's traversability based on the robot's instantaneous proprioceptive feedback (e.g., soil feels increasingly deformable and is nontraversable). The current proprioception map is constructed by extrapolating the robot's present proprioceptive measurements to predict upcoming traversability along the robot's trajectory. This map relies solely on the proprioceptive feedback, which is inherently reliable regardless of environmental conditions that affect visual sensors. The traversability cost is calculated based on the distance from the robot's current location, with a predefined cost for moderately traversable terrain adjusted by the observed proprioceptive signals [8].

Adaptive Coupling

AMCO combines the general knowledge map, traversability history map, and current proprioception map into a final cost map C_{amco} based on the reliability (ξ) of the visual sensor data. This reliability is assessed using metrics such as brightness and motion blur, which impact the accuracy of the semantic segmentation. The coupling mechanism assigns weights to the vision-based general knowledge and recent history maps according to the reliability score and integrates them with the proprioception map to form the coupled traversability cost map.

$$C^t_{amco} = \xi.\left(C^t_{general} + C^t_{history}\right) + C^t_{prop}. \quad (1)$$

C_{amco} (Figure 1 [right]) is used as a robot-centric local cost map that can be used to compute least-cost robot trajectories and gaits using a planning algorithm [11]. It ensures that navigation decisions prioritize the most reliable sensory input, adapting to varying environmental conditions.

Perceiving and Navigating Well-Separated Vegetation

To estimate the traversability of different kinds of vegetation, navigate cautiously under uncertainty, and recover from physical entrapments in vegetation, VEgetation-aware Robot Navigation [VERN] [7] is presented. VERN uses RGB images and 2-D laser scans to classify vegetation based on pliability (a measure of how easily a robot can walk through them) and presents cautious navigation strategies for vegetation. VERN's key components and how they connect are discussed in the following subsections and shown in Figure 2.

In the figure, the few-shot classifier uses quadrants of RGB images

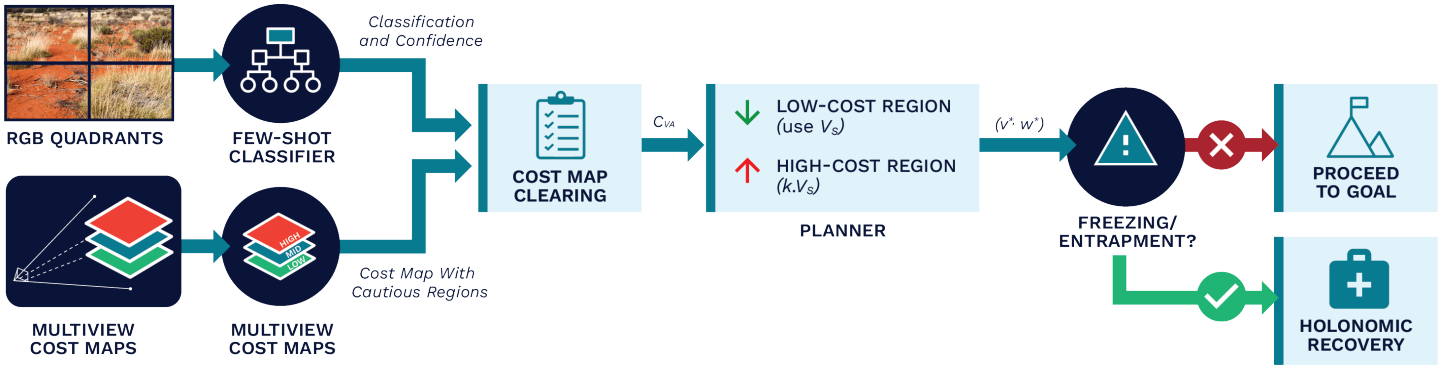

Figure 2. Overall System Architecture of VERN [7] *(Source: K. Weerakoon).*

> ***VERN uses RGB images and 2-D laser scans to classify vegetation based on their pliability and presents cautious navigation strategies for vegetation.***

and compares them with reference images of various vegetation classes to output a vegetation class and confidence. Multiview cost maps corresponding to various heights are used to assess vegetation height. Using the classification, confidence, and height, the costs are cleared/modified to enable the robot to walk through PV if necessary. Further, if the robot freezes or gets entangled in vegetation, it resorts to holonomic behaviors to reach a safe location that is saved prior to freezing.

Few-Shot Learning Classifier

VERN employs a few-shot learning classifier based on a Siamese network architecture [12] to detect various kinds of vegetation with high accuracy using limited RGB training data. This classifier is trained on a few hundred RGB images to classify vegetation as tall grass, bushes, or trees, each with distinct pliability characteristics. During training, the classifier is fed with pairs of images either belonging to the same or different vegetation class. Thus, the classifier learns to compare images and identify similar types of vegetation. During runtime, the classification process begins by dividing the RGB image into quadrants. Each quadrant is compared with reference images to detect the type of vegetation present. The classifier finally groups vegetation binarily into the following two main types:

1. PV: Vegetation that the robot can navigate through (grass of different heights and densities).
2. Nonpliable vegetation (NPV): Vegetation that the robot must avoid (trees and bushes).

Multiview Cost Maps

To detect vegetation height and density accurately, VERN uses three tiers of cost maps derived from 2-D LiDAR scans at different heights. These cost maps, represented as C_{low}, C_{mid}, and C_{high}, have the following properties. C_{low} captures all obstacles, providing a base map for general navigation. C_{mid} focuses on medium-height obstacles like bushes and low-hanging branches. C_{high} captures tall obstacles such as trees and buildings. Using multiple layers helps distinguish between critical obstacles (e.g., trees and buildings) and noncritical elements like overhanging foliage, allowing for safer navigation decisions.

Integrating Classification and Cost Maps

Using homography, the RGB quadrants passed to the classifier are projected onto the multiview cost maps to align the vegetation data recorded in the image and cost map and create a vegetation-aware traversability map (CVA). This map guides the robot's navigation decisions by dynamically

adjusting the navigation costs based on the vegetation's pliability, height, and classification confidence. For instance, short and high-confidence PV has a lower cost, promoting navigation through these areas. Taller and less PV has a higher cost, encouraging the robot to avoid them. VERN uses the dynamic window approach to navigate different vegetation types by dynamically computing the least-cost robot's linear and angular velocities based on CVA.

Cautious and Recovery Behaviors

When encountering high-cost or uncertain regions in the traversability map, VERN executes cautious navigation behaviors by limiting the robot's maximum velocity to prevent collisions. Further, VERN includes recovery behaviors for situations where the robot gets physically entrapped in dense vegetation by storing safe locations as the robot navigates. The robot can extricate itself from entanglements using holonomic movements to the closest safe location.

Perceiving Intertwined Vegetation

When pliable and NPV are highly intertwined with each other, RGB image-based methods such as VERN could produce erroneous classifications that could lead to collisions. To overcome this limitation, multilayer intensity maps (MIMs) [13] are proposed. Although LiDAR point clouds (represented as [x, y, z, int]) scatter in the presence of thin, unstructured vegetation like tall grass, the intensity (int) of the light reflected back to the LiDAR indicates the object's solidity properties (higher intensities implies higher solidity). MIMs utilize this property to differentiate PV intertwined with nonpliable obstacles, as the reflected intensities would be high.

MIMs

MIMs [13] are composed of several layers of 2-D grid maps (see Figure 3). Each of these layers is constructed by (1) discretizing the x, y 3-D point cloud points into grid locations, (2) summing the intensity of all the points within a grid and height interval, and (3) normalizing the summed intensity and assigning its value to a grid. Therefore, each layer would contain grids with various intensity values at various locations around the LiDAR. This denotes the solidity of the objects, and implicitly, also their height.

In the figure, the intensities contained in the grids of each layer are compared against a threshold intensity. If the intensities are lower than the threshold, this indicates the presence of a nonsolid or pliable object. This information is finally fed into a planner for navigation.

Detecting Intertwined Vegetation

To differentiate truly solid, dense vegetation (e.g., trees and bushes) from PV like tall grass, three layers of MIMs are used. The three grids correspond to three nonoverlapping height intervals from the ground to the maximum height that the LiDAR can view. The grids of each of these layers are summed, and each grid's value

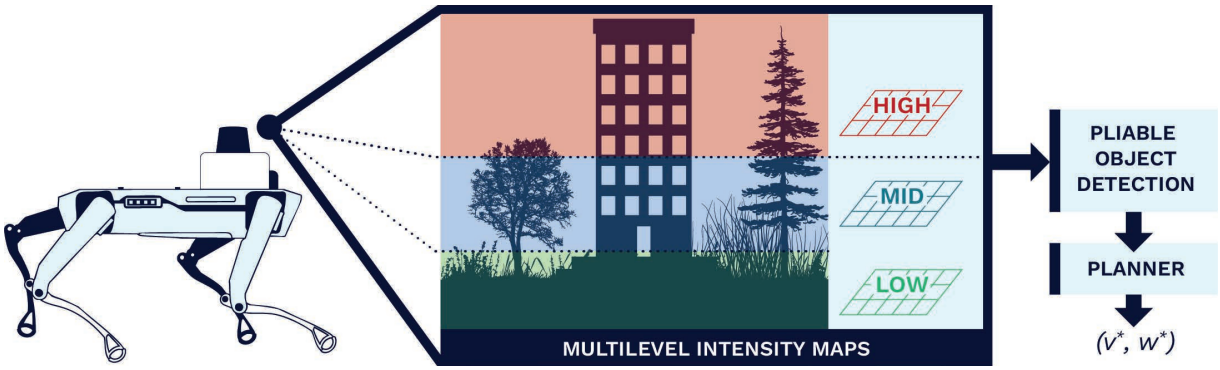

Figure 3. MIM Layers Using the Point Clouds Corresponding to Different Height Intervals *(Source: K. Weerakoon)*.

is checked to see if it is greater than an intensity threshold. If it is, then the grid corresponds to a truly solid vegetation like a tree. If not, then it belongs to either free space or PV like tall grass.

Since MIMs also view different height levels, the reflected higher intensities will allow them to be detected as truly solid obstacles, even if PV is intertwined with taller solid obstacles. Additionally, since MIM layers use a grid map structure, they can be directly used as cost maps for planning low-cost robot trajectories.

> ***Since MIM layers use a grid map structure, they can be directly used as cost maps for planning low-cost robot trajectories.***

Real-World Evaluation

All these methods have been implemented on a real Boston Dynamics Spot robot and evaluated on real-world unstructured terrains and vegetation compared to prior works such as GA-Nav [9] and Spot's Inbuilt planner (see Figure 4).

FUTURE WORK

There are several challenges unaddressed by existing work in navigating unstructured vegetation beyond those discussed in the "Challenges in Unstructured Outdoor Navigation" section. These challenges are discussed next, and a few potential solutions for addressing them are proposed.

Robust Detection of Diverse Vegetation

Although VERN and MIM introduce preliminary methods to detect vegetation pliability, the large diversity of vegetation appearances and other obstacles (e.g., barbed wire fences that MIMs may not be able to detect) necessitates developing novel, robust perception methods. To this end, compact vision language models (VLMs) such as Contrastive Language-Image Pretraining [14] are promising and can be fine-tuned using real-world data of different kinds of vegetation and obstacles to robustly detect them.

Handling Positive and Negative Obstacles

Positive obstacles are referred to here as those that the robot can climb, jump, or leap over instead of circumventing them (e.g., mounds, fallen branches, logs, etc.). Negative obstacles are ditches, pits, and potholes that could destabilize the robot. Traversing environments with such obstacles requires superior perception and locomotion capabilities. Fusing RGB image-based segmentation or classification [9, 15, 16] and LiDAR point clouds could help estimate the types and dimensions of such obstacles when they are unoccluded by entities

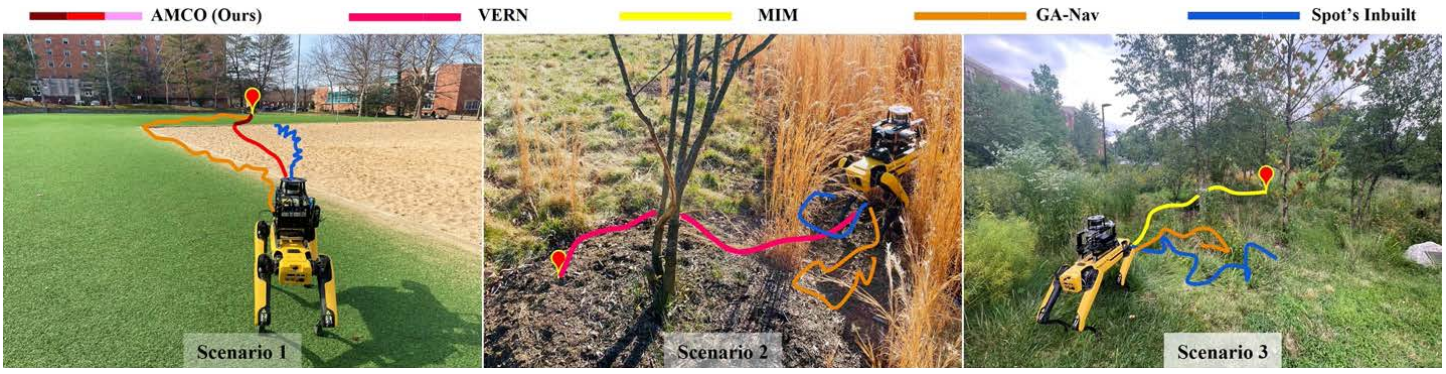

Figure 4. Navigation Trajectories Generated by AMCO [8], VERN [7], and MIM [13] in Diverse Vegetation and Terrain Scenarios *(Source: M. Elnoor)*.

like vegetation. However, when they are occluded by vegetation, using proprioceptive feedback and novel locomotion policies trained using deep reinforcement learning (DRL) could help detect such obstacles and maintain stability while traversing them.

Handling Adverse Lighting and Weather

Adverse lighting and weather conditions can significantly impact the robot's exteroceptive perception capabilities. Low light or harsh sunlight can obscure visual data, making it difficult for the robot to detect and navigate obstacles. A few possibilities to address adverse lighting are as follows:

- Altering the lighting in the images used to train compact VLMs for detecting various obstacles.
- Relying more on point cloud and proprioception in poorly lit scenarios.
- Developing probabilistic methods to predict the traversability of terrains ahead based on past elevation, proprioception data.
- Training DRL locomotion policies to exhibit cautious behaviors such as gently bumping into objects using the front legs to assess the upcoming terrain's traversability.

To address adverse weather, methods to handle occlusions caused by rain droplets or snow on cameras and LiDAR sensors can be developed. This involves assessing affected parts of images or point clouds and relying on unaffected data for perception. Additionally, complementing exteroception with proprioception can ensure reliable traversability estimation under partial observability.

Handling Water Bodies

Compared to wheeled robots, legged robots can traverse still and running water of certain depth (e.g., knee deep) due to their superior dynamics. Still water, apart from exerting resistance to the robot's motion, could also present occluded, slippery terrains with rocks, pebbles, soil, etc., on the waterbed. Therefore, the primary challenge is to detect these poor foothold and granular challenges using proprioceptive feedback and developing new locomotion strategies to stabilize and walk on such terrains. A possible solution is to use online and offline DRL approaches for training a blind (without exteroception) locomotion policy with trials on simulated pebbles, rocks, and still water (higher resistance to leg motion) first and then fine-tuning the model with real-world data. Suggesting a blind locomotion policy first ensures that the robot can traverse terrains even when all exteroceptive inputs become unreliable.

Running water poses additional challenges due to various resistive forces and slippery, rocky riverbeds. To address this, methods to estimate the overall water flow (direction and magnitude), along with the properties of the underlying terrain using the forces experienced by the robot's knee and hip joints, can be developed. Next, the feasibility of traversing through the water stream is estimated by transforming the water flow and underlying waterbed's traversability into the motor torque requirements. If the requirements are lower than the maximum torques that the robot can generate, the stream is considered traversable.

> ***Compared to wheeled robots, legged robots can traverse still and running water of certain depth due to their superior dynamics.***

CONCLUSIONS

In this article, some of the challenges of navigating a legged robot on unstructured outdoor terrains with a variety of terrain properties and vegetation were discussed. Solutions were proposed using exteroceptive and proprioceptive sensing to perceive a terrain's properties and adapt the robot's velocities and gaits for stable navigation. Furthermore, RGB

image-based and LiDAR point cloud-based methods accurately detecting vegetation properties like pliability were analyzed.

Outdoor environments pose many more challenges to navigation. Several key problems like the diversity of vegetation, small positive and negative obstacles on the ground, and still/running water were addressed, as well as potential directions for future work in perception and locomotion. ■

REFERENCES

[1] Bruzzone, L., and P. Fanghella. "Functional Redesign of Mantis 2.0, a Hybrid Leg-Wheel Robot for Surveillance and Inspection." *Journal of Intelligent and Robotic Systems*, vol. 81, pp. 215–230, 2016.

[2] Khan, A., C. Mineo, G. Dobie, C. Macleod, and G. Pierce. "Vision Guided Robotic Inspection for Parts in Manufacturing and Remanufacturing Industry." *Journal of Re-Manufacturing*, vol. 11, no. 1, pp. 49–70, 2021.

[3] Matthies, L., Y. Xiong, R. Hogg, D. Zhu, A. Rankin, B. Kennedy, M. Hebert, R. Maclachlan, C. Won, T. Frost, et al. "A Portable, Autonomous, Urban Reconnaissance Robot." *Robotics and Autonomous Systems*, vol. 40, no. 2-3, pp. 163–172, 2002.

[4] Yoshiike, T., M. Kuroda, R. Ujino, H. Kaneko, H. Higuchi, S. Iwasaki, Y. Kanemoto, M. Asatani, and T. Koshiishi. "Development of Experimental Legged Robot for Inspection and Disaster Response in Plants." The 2017 IEEE/RSJ International Conference on Intelligent Robots and Systems (IROS), IEEE, pp. 4869–4876, 2017.

[5] Valsecchi, G., C. Weibel, H. Kolvenbach, and M. Hutter. "Towards Legged Locomotion on Steep Planetary Terrain." The 2023 IEEE/RSJ International Conference on Intelligent Robots and Systems (IROS), IEEE, pp. 786–792, 2023.

[6] Frey, J., M. Mattamala, N. Chebrolu, C. Cadena, M. Fallon, and M. Hutter. "Fast Traversability Estimation for Wild Visual Navigation." arXiv preprint arXiv:2305.08510, 2023.

[7] Sathyamoorthy, A. J., K. Weerakoon, T. Guan, M. Russell, D. Conover, J. Pusey, and D. Manocha. "VERN: Vegetation-Aware Robot Navigation in Dense Unstructured Outdoor Environments." The 2023 IEEE/RSJ International Conference on Intelligent Robots and Systems (IROS), IEEE, pp. 11 233–11 240, 2023.

[8] Elnoor, M., K. Weerakoon, A. J. Sathyamoorthy, T. Guan, V. Rajagopal, and D. Manocha. "AMCO: Adaptive Multimodal Coupling of Vision and Proprioception for Quadruped Robot Navigation in Outdoor Environments." arXiv preprint arXiv:2403.13235, 2024.

[9] Guan, T., D. Kothandaraman, R. Chandra, A. J. Sathyamoorthy, K. Weerakoon, and D. Manocha. "GA-Nav: Efficient Terrain Segmentation for Robot Navigation in Unstructured Outdoor Environments." *IEEE Robotics and Automation Letters*, vol. 7, no. 3, pp. 8138–8145, 2022.

[10] Elnoor, M., A. J. Sathyamoorthy, K. Weerakoon, and D. Manocha. "ProNav: Proprioceptive Traversability Estimation for Autonomous Legged Robot Navigation in Outdoor Environments." arXiv preprint arXiv:2307.09754, 2023.

[11] Fox, D., W. Burgard, and S. Thrun. "The Dynamic Window Approach to Collision Avoidance." *IEEE Robotics Automation Magazine*, vol. 4, no. 1, pp. 23–33, March 1997.

[12] Koch, G. R., R. Zemel, and R. Salakhutdinov. "Siamese Neural Networks for One-Shot Image Recognition." Proceedings of the 32nd International Conference on Machine Learning, Lille, France, 2015.

[13] Sathyamoorthy, A. J., K. Weerakoon, M. Elnoor, and D. Manocha. "Using LiDAR Intensity for Robot Navigation." arXiv e-prints, p. arXiv:2309.07014, September 2023.

[14] Radford, A., J. W. Kim, C. Hallacy, A. Ramesh, G. Goh, S. Agarwal, G. Sastry, A. Askell, P. Mishkin, J. Clark, G. Krueger, and I. Sutskever. "Learning Transferable Visual Models from Natural Language Supervision." arXiv e-prints, p. arXiv:2103.00020, February 2021.

[15] Song, Y., F. Xu, Q. Yao, J. Liu, and S. Yang. "Navigation Algorithm Based on Semantic Segmentation in Wheat Fields Using an RGB-D Camera." *Information Processing in Agriculture*, vol. 10, no. 4, pp. 475–490, 2023.

[16] Wang, W., B. Zhang, K. Wu, S. A. Chepinskiy, A. A. Zhilenkov, S. Chernyi, and A. Y. Krasnov. "A Visual Terrain Classification Method for Mobile Robots' Navigation Based on Convolutional Neural Network and Support Vector Machine." *Transactions of the Institute of Measurement and Control*, vol. 44, no. 4, pp. 744–753, 2022.

BIOGRAPHIES

ADARSH JAGAN SATHYAMOORTHY is a researcher focusing on developing navigation algorithms for mobile robots operating in densely crowded indoor and unstructured outdoor environments. Dr. Sathyamoorthy holds a Ph.D. in electrical and computer engineering from the University of Maryland, College Park.

KASUN WEERAKOON is a Ph.D. student in the Electrical and Computer Engineering Department at the University of Maryland, College Park, where he researches developing autonomous navigation algorithms using machine-learning techniques for mobile robots operating in complex outdoor environments.

MOHAMED ELNOOR is a Ph.D. student in the Electrical and Computer Engineering Department at the University of Maryland, College Park, where he researches autonomous robot navigation in challenging indoor and outdoor environments.

JASON PUSEY is a senior mechanical engineer at the U.S. Army Combat Capabilities Development Command Research Laboratory, with 20 years of robotics experience. He is recognized as the U.S. Department of Defense's subject matter expert on legged robotics, having led multiple programs advancing the state of the art of legged robotics. Mr. Pusey holds undergraduate and graduate degrees in mechanical engineering from the University of Delaware.

DINESH MANOCHA is a Paul Chrisman-Iribe chair in the Computer Science, Electrical, and Computer Engineering Department and distinguished university professor at University of Maryland, College Park. His research interests include virtual environments, physically-based modeling, and robotics. He has published more than 750 papers and supervised 50 Ph.D. dissertations. He is a fellow of Association for the Advancement of Artificial Intelligence, American Association for the Advancement of Science, Association for Computing Machinery (ACM), and Institute of Electrical and Electronics Engineers and an National Academy of Inventors member of the ACM SIGGRAPH Academy. He received the B´ezier Award from the Solid Modeling Association, the Distinguished Alumni Award from IIT Delhi, and the Distinguished Career Award from Washington Academy of Sciences. Dr. Manocha holds a B.Tech. from the Indian Institute of Technology, Delhi, and a Ph.D. in computer science from the University of California at Berkeley.

MICRODIODE LASER PRIMERS – A PATH FORWARD

BY STEPHEN REDINGTON AND GREGORY BURKE

(PHOTO SOURCE: DIGITAL ART RENDERING [123RF.COM])

INTRODUCTION

The concept of using lasers to ignite propellant and energetic material is not new. At the U.S. Army Combat Capabilities Development Command-Armaments Center (DEVCOM-AC) at Picatinny Arsenal, NJ, the Army explored efforts to use external mounted lasers for medium- and large-caliber weapons systems, with modest success in the 1980s through 2010.

Early on, compact, solid-state, laser diode technology was an obvious solution but was in its infancy, costly, and an immature technology. Low-cost, high-volume production of microdiode laser manufacturing matured in the late 1980s, and the technology has continually been improving ever since.

Microlaser chips make it possible to fit the entire laser assembly into the munition itself as a onetime use, disposable component. This eliminates external optics, simplifies assembly, improves reliability, and avoids the problems associated with directing a laser beam through the gun breach. What makes microdiode laser ignition technology attractive is that it can be made seamlessly and interchangeably with existing electrically fired gun platforms without modification.

With advances in electronics and new threats from electronic warfare, the benefits of microdiode laser ignition are becoming clear. Older, established electrical ignition technology is susceptible to the ever-increasing use of electromagnetic-radiation-producing devices (e.g., radar, directed energy weapons, etc.) on the battlefield. This is especially true on U.S. Navy ships that use high-powered radar near other onboard weapons systems. The effect of such radiation is known as Hazards of Electromagnetic Radiation on Ordnance (HERO), and its effect on a munition may require special procedures for munition handling. HERO testing of microdiode laser ignition devices has demonstrated these devices to be less susceptible or even immune for several reasons. The first is due to its inherent high (electrical) energy threshold required to produce the optical output (lasing action) required for ignition.

A second is that the electronics are physically isolated from the energetics so there is no accumulation of heat in the energetics. This is not the case for the established electrical ignition technology where the conducting media (heating element) is embedded within or is a part of the energetic material.

Work on applying surface mount, electronic manufacturing technology to 30-mm ammunition began in 2015 at the Fuze Development Center (FDC) at Picatinny Arsenal. The FDC is well suited for this task, as its mission is to transition research and development (R&D) prototypes to manufacturing and ultimately to the field. It also has a capability for state-of-the-art surface mount technology (SMT) fabrication and assembly required for proving manufacturability in the private sector. The effort to use SMT on microdiode laser technology has been successful, leading to many government-owned patents on the technology and a contract with two cartridge manufacturers to qualify the technology for 30-mm applications.

> ***With advances in electronics and new threats from electronic warfare, the benefits of microdiode laser ignition are becoming clear.***

TODAY'S ELECTRICALLY INITIATED DEVICES

Most of the HERO issues are related to an electrical-based ignition technology developed in the early 1900s. A resistive-heating element generates heat to start the ignition process. This element is often referred to as a bridgewire or

conductive mix, which, in some cases, is the energetic material itself.

This heating element is typically in close contact with the energetic material to maximize heat transfer to produce the fastest possible initiation time. This is particularly important in high-rate-of-fire applications ranging from 600 to 3,000 rounds per minute or higher. Prolonged exposure to electrical and/or radio frequency (RF) fields can create currents that may cause this resistive element to generate heat. Even when this current is not sufficient to initiate the embedded energetic material, long-term exposure to these fields (or heat in some cases) can chemically alter the nature of the energetic material, resulting in changes to the response times and/or sensitivity of these materials. This may damage the ammunition or increase ignition susceptibility, which could increase risk during ammunition handling. This problem is not limited to ammunition.

Other ordnance such as countermeasure flares used on fighter aircraft, cartridge/propellant-actuated devices (CADs/PADs), and detonators for explosives are also affected. Because bridgewire technology operates on heat generated from electrical resistance, Ohm's law applies. This law dictates that the heat produced will be proportional to the current passing through the resistive element. A solution to the HERO problem is to find another way to transfer heat to the energetic material. Microdiode laser ignition can be a solution to these problems.

WHY MICRODIODE LASER PRIMERS?

The Navy is particularly interested in alternatives to conventional electrical ignition due to the potential susceptibility of electrically primed munitions to HERO aboard ship. While the prior work focused on 30-mm machine guns, recent activity is focusing on expanding the technology to include 20-mm platforms as well as other CAD/PAD systems. Personnel and helicopter electrostatic discharges (PESDs and HESDs) are also a concern. The HERO susceptibility problem has spread beyond Navy ships and now affects all services that handle munitions or explosives in all battlefield environments.

Microdiode laser ignition transfers heat in the form of infrared radiation. This can be done without making direct physical contact with the energetic material. Furthermore, lasers require a minimum energy barrier be exceeded before any coherent optical energy output can be produced and the resulting energy transferred to the energetics. This means that prolonged exposure to an electrical or RF field minimizes heat transfer to the energetic material if the munition is properly designed. The electrical current required for laser initiation is typically above 1 A or more, which is typically 2–3 times more than conventional, electrical ignition devices. It is also possible to further raise this current/energy threshold well above any possibility for unintended initiation in almost any HERO environment if the weapons platform can deliver enough current to the device to activate the laser.

> ***The Navy is particularly interested in alternatives to conventional electrical ignition due to the potential susceptibility of electrically primed munitions to HERO aboard ship.***

THE PAST

In 2015, work began at Picatinny Arsenal to realize the concept of replacing the resistive bridgewire component of an electrically energized munition with a disposable microdiode laser. The 30-mm ammunition was the target application, as this ammunition is known to have HERO safety and PESD/HESD issues aboard Navy ships. There is also a strong incentive to explore and develop alternatives to solve this problem. Enough research had been done at that time to realize a microdiode laser

primer could be made to seamlessly interchange with an existing 30-mm gun platform ammunition.

There were two immediate problems for adapting this technology into the existing primer cup. The first was soldering edge-emitting diodes on opposite sides of the chip, i.e., soldering top to bottom rather than a bottom-only surface, as in typical surface mount components. This problem is typically solved by wire bonding from the top surface to a bottom surface. A more robust, low-cost, mass-producible solution was desired for ammunition. This is largely due to the harsh shock, vibration, and temperature environment of the ammunition. It is also important to control cost for ammunition production. These rates can scale from thousands to millions of units per month.

The second problem was adapting the edge-emitting laser to fire vertically into the 30-mm flash tube located above the primer. This is not possible if the laser is mounted horizontally on a printed circuit board (PCB). An answer to these problems was the flex mount technology, as illustrated in patent 9,618,307, "Disposable, Miniature Internal Optical Ignition Source for Ammunition Application" [1] (see Figures 1–3). The technology allowed the laser to be mounted so its output was directed vertically while being soldered to a horizontal surface. It also provided the ability to adapt the laser height vertically to minimize the air gap from the laser facet to the next assembly—the flash tube in the 30-mm case. This allowed the primer to be nonenergetic while the cartridge's manufacturing and assembly were done by existing facilities with specialized safety protocols.

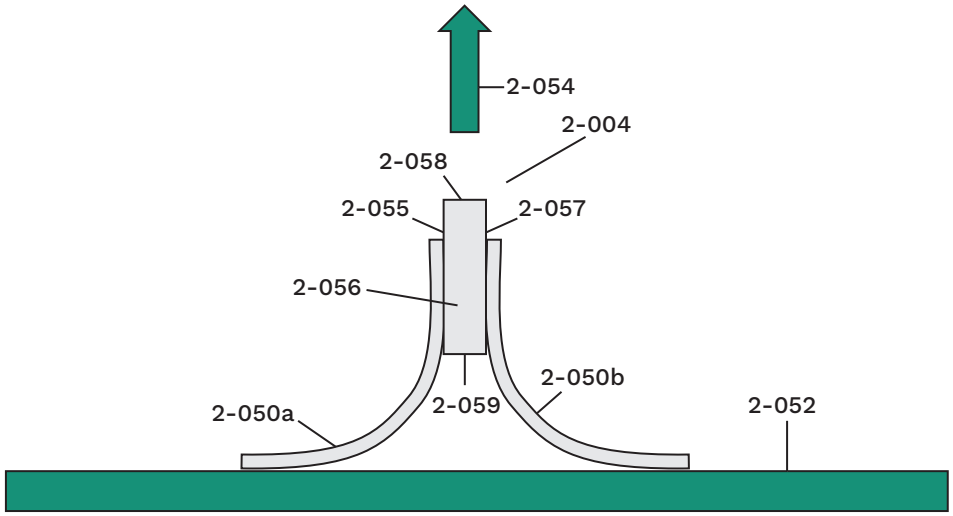

Figure 1. Laser Flex Mount *(Source: S. Redington et al. [1])*.

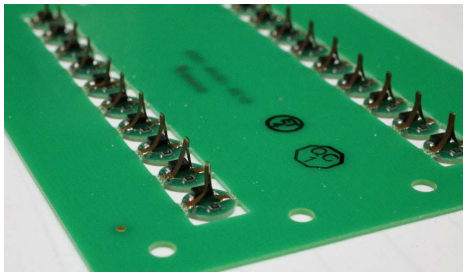

Figure 2. First SMT Laser Primers Assembled in 2017 *(Source: S. Redington)*.

Figure 3. Nonpolarized Laser *(Source: S. Redington)*.

A nonenergetic laser primer can be manufactured at any conventional contract manufacturing facility that can assemble SMT. In addition, a nonenergetic primer can be 100% tested before shipping to the cartridge assembly facility. This is not possible with existing bridgewire technology. As such, these two features were seen as benefits to the 30-mm application.

By 2017, the first functional microdiode lasers were produced on the FDC surface mount assembly line. This introduced a new generation of electronic primer with surface mount electronics embedded in place of energetic material. This capability also allowed more functionality to be incorporated in the basic primer itself. An internal continuity check and RF energy shunt features were added to the design. These early units were built up into PA520 primer cups (as shown in Figure 4), assembled into 30-mm cartridges, and successfully demonstrated as fully functional

Figure 4. The First Microdiode Laser Primers *(Source: S. Redington)*.

equivalents of existing 30-mm ammunition. It was later learned that such gun platforms were deployed with two differing electrical power configurations—one with the chassis connected to the positive terminal of the power source and another with the chassis connected to the negative terminal. The first primer design was a unipolar configuration. That meant there was no way to ensure operation on any fielded platform.

Because unipolar operation is an inherent property of all diodes, the laser diode is no exception. To eliminate this problem, the next generation design incorporated a full-wave rectifier, along with the continuity check and energy shunt features. The new design proved that more electronic functionality could be added to primer technology than just ignition alone. This gave way to the possibility of more advanced concepts like smart primers. These primers could embed memory, temperature sensors, and lock mechanisms that would enable security to be built into the ammunition itself. All these features were described in patent 10,415,942, "Disposable, Miniature Internal Optical Ignition Source," granted in 2019 [2]. At that time, work began on applying the technology to 20-mm, electrically primed ammunition.

Extensive testing of the 30-mm laser primers revealed a weakness of microdiode laser primers. That weakness was with firing systems that utilize capacitive discharge as a means of energizing the primer. Unlike the target 30-mm firing platform, these systems have extremely low source impedance to maximize current through the primer. The target 30-mm platform has a built-in, 100-ohm impedance that limits the discharge current applied to the primer. Unfortunately, diodes do not handle unrestricted current flow very well or not at all. In the target's case, the 100-ohm impedance restricts the current to a 1.5-A maximum. This works well for the laser diode selected for the 30-mm target application. Later experiments with capacitive discharge systems showed the discharge currents could reach 80 A or higher, albeit for an extremely brief period. Unlimited current tends to destroy the laser before it has a chance to output any laser energy. This presents a problem for advancing the technology beyond the target 30-mm application.

> ***Extensive testing of the 30-mm laser primers revealed a weakness of microdiode laser primers.***

THE PRESENT

An important design consideration for a microdiode laser primer is that the microdiode laser acts like a one-time, single-use electrical fuse. In that respect, traditional design for reliability does not apply. For example, lasting thermal effects that would otherwise prohibit use of a laser diode can be totally ignored. As a result, bulky heat sink mechanisms are not required for a laser primer to perform its one-time function. This simplifies the design and allows a greater potential for microminiaturization.

The design requirement to consider is that the diode performs its mission before it self-destructs. This is relatively easy to do for a power source with a built-in impedance and has been demonstrated on the Apache platform. Ignition was achieved in the first versions of laser primers, with less than one millijoule of input energy in less than 100 µs. Uncontrolled impedance sources present a very different circumstance due to their high-current, short-duration pulse. The problem is that the diode fails before the device can deliver useable laser energy or the pulse is so short that there is not enough time to achieve ignition. In this case, reliability is a race against time.

Work began late in 2019 to develop a new circuit concept to adapt the technology to the capacitive discharge supplies. The challenge for smaller-caliber applications like the 20 mm is that there is no flash tube in the cartridge. Flash tubes are required in larger-caliber munitions to boost the propellant ignition point deeper into the center of the cartridge rather than lighting the propellent from one end. This greatly reduces the time to burn all the propellent. The 30-mm flash tube allows the primer to be completely inert since all the ignition requirements can be met by a flash tube modified to accept the laser input. This combination makes up for the lost energetic material in the PA520 primers used in producing 30-mm ammunition. This is not possible

Flash tubes are required in larger-caliber munitions to boost the propellant ignition point deeper into the center of the cartridge.

when there is no flash tube, as in the case of small-caliber ammunition.

The primer itself must contain sufficient energetic material to boost the ignition output fast enough to completely ignite the propellant. This reaction time is a factor that must be considered since this must be done within the time required to fire the next bullet. Replacing the bridgewire with electronics severely limits the available space if that space needs to be shared with energetic material to meet performance requirements. Firing the laser vertically into an adjacent flash tube is out of the question for small-caliber applications since there is no flash tube.

These new problems led to the concept and development of radially fired laser technology. The benefit of the radially fired design is that energetic material can be contained in a center cavity at the bottom of the primer. This material is initiated from the side as opposed to above. This creates space in the primer cup for energetic material lost in the flex mount design. The energetic material can also be completely isolated from the electronics' direct contact by encapsulating the circuit assembly in an optically clear epoxy.

The first radially fired laser was developed late in 2019 and is shown in Figure 5. A second, more-refined version is shown on the right and was produced later that year. The primary difference was a castellated solder joint for soldering the PCB to the primer cup side walls rather than the unsupported solder joint of the original design. This new design incorporated a high level of integration in a smaller space than previous designs. Not only was the full wave bridge rectifier and continuity check incorporated, but a load bank and transient voltage suppressor were added to dissipate the excess energy

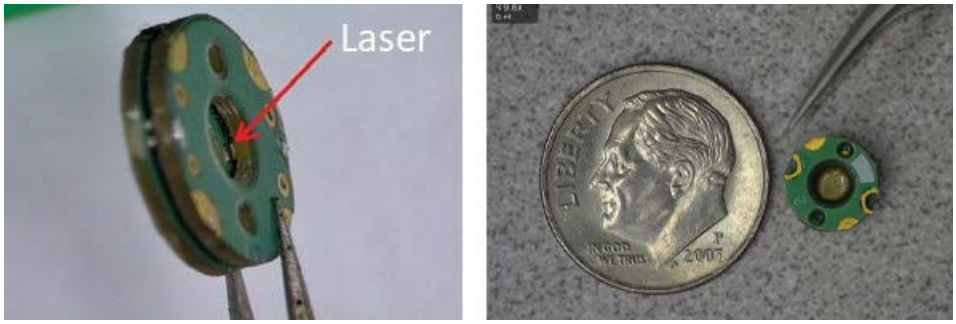

Figure 5. Radially Fired Laser *(Source: S. Redington).*

of a capacitive discharge supply. This design was created to function in 30- and 20-mm applications. The radially fired laser was successfully demonstrated and patented in 2022.

A problem with capacitive discharge firing supplies is the amount of excess energy they deliver. This energy must be dissipated to protect the laser long enough to successfully ignite the energetic material. To complicate matters, the amount of this excess energy depends on the specific gun platform in use. Testing of the latest version indicates the design is compatible with the target 30-mm platform, along with capacitive discharge energy levels typical of older, existing platforms.

> ***A problem with capacitive discharge firing supplies is the amount of excess energy they deliver.***

The complication of evaluating the design for all platforms lies in the stored potential energy of the firing circuit. Given that the current of the discharge is unlimited by any significant series resistance, the total energy that must be handled by the laser primer is given by the formula $1/2 \times C \times V^2$. Both the capacitance (C) and voltage (V) depend on the specific gun platform. The challenge is that the energy is proportional to the square of the voltage.

Testing done on the 2022 design indicated it was likely to work for many capacitive discharge supplies currently fielded; however, there are exceptions. When a developmental 20-mm platform was studied, it was found that the firing voltage could reach as high as 315 V, with 3 μF of capacitance (149 mJ). This is an unprecedented energy level and one that the 2022 design is unable to handle. The underlying problem is dissipating that much excess energy in such a small, confined space.

It should be noted that a 250-V, 3-μF capacitance energy level (95 mJ) was successfully demonstrated. This indicates a solution is possible. Clearly, understanding the firing circuit issues and challenges has dramatically improved from the early designs. More investment is needed to develop a general design capable of being quickly adapted to function in the myriad of capacitive discharge firing circuits in existing platforms.

THE FUTURE

Enough R&D has been performed to show microdiode laser ignition has a future in applications where HERO, PESD, and HESD safety are a concern. The technology directly applies to electrically primed, small- and medium-caliber ammunition and artillery. There is also potential to improve testability and reliability in critical applications such as countermeasure flares, squibs, and CAD/PAD applications (see Figure 6). Placing electronics in the primer cup can also enable smart ammunition. These are munitions that could use one-wire technology to communicate to the platform or user for information or control. Beyond that, applications like HERO safe replacements for electrically initiated detonators are possible.

Laser ignition has been shown to work in an M6 blasting cap, demonstrating potential applications in demolitions. This would also suggest an M100 detonator replacement is possible. Many of these applications require a continued investment to adapt the technology to capacitive-discharge-type firing power supplies. The challenge is to adapt the discharge current to match the laser diode's capability. This must be done in the smallest amount of space with two aspects: (1) hold off a large amount of excess energy and stretch it out over time and (2) do this in an extremely small volume.

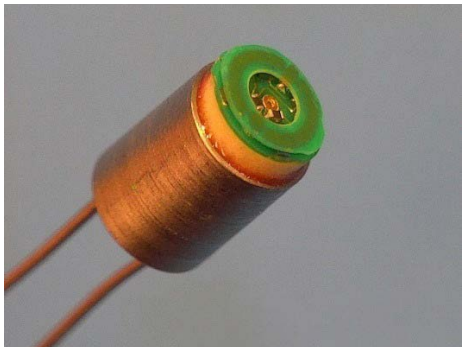

Figure 6. Microminiaturized Bipolar Laser *(Source S. Redington)*.

A practical goal for the future is a common basic design that would be suitable for as many applications as possible. A design that can handle capacitive-discharge-type firing supplies is key but not a limiting factor.

Fuzing is a potential application where the electronics design can adapt to the laser technology. This is because each fuze application functions as its own, self-contained system. Backward compatibility with an existing weapons platform is not an issue in this case. As such, the impedance source can be made to match the laser diode; capacitive discharge is not an issue. This would also be true of new, emerging applications. This means that despite the problems encountered with capacitive power sources, the future of laser primer technology is still promising.

GETTING MICRODIODE LASER TECHNOLOGY TO THE FIELD

Backwards compatibility with existing platforms is a requirement for any new electric primer technology. In virtually every case, retrofitting existing platforms would be extraordinarily expensive and highly undesirable. In addition, any solution that prevents the prior technology from being used would not be practical or accepted. Continued R&D must be explored for microdiode laser ignition to become a viable, cost-effective alternative to current electrical-based ignition devices. For example, in the high rate of fire for 20-mm ammunition applications, this technology necessitates a high volume/low-cost end item to be a realistic alternative to existing technology. A major cost driver of this technology is the cost of the laser diode.

> ***Continued R&D must be explored for microdiode laser ignition to become a viable, cost-effective alternative to current electrical based ignition devices.***

Studies show that it is possible to mass produce such laser diodes within an acceptable price point to be practical for the mass production rates of most ammunition. This is proven by the low cost of diode laser devices used in compact disc players, laser pointers, and automotive light detection and ranging. These low-cost laser diodes are readily available from suppliers in Asia. Unfortunately, the United States no longer possesses a manufacturing capability for low-cost, laser diode technology, as the offshore availability of these lasers is plentiful. There is currently no market influence in this country to increase production or reduce cost for onshore production.

The COVID pandemic has exposed the United States' dependence on foreign technology for military and commercial markets. This is particularly troublesome for military markets, as tensions rise with China. The U.S. government has recognized the problem and responded with the CHIPS and Science Act of 2022, which supports domestic production of semiconductors.

Regardless of the supply chain issue, increasing demand for diode lasers is essential for lowering manufacturing cost. Military applications would tend to demand a domestic supply be developed. Such application areas could be initiating devices used in artillery, demolition, or CAD/PAD devices, as well as similar devices within the commercial sector like automotive air bags, fire extinguishers, or mining.

One application explored was a potential primer M123 replacement used in artillery. Another was a laser-initiated M6 blasting cap. Both applications showed potential for the technology. Use in countermeasure flares and CAD/PAD devices was also explored briefly. Enough development was done to show promise; however, a primer that can work with capacitive discharge firing systems is required for many of these applications.

CONCLUSIONS

In summary, microdiode laser technology has a lot to offer across a span of multiple platforms. Low-cost, high-volume production is possible for military and commercial applications. There are many new applications that could be enabled by this technology, such as smart ammunition, nonenergetic tracers, time-delayed functions, and more. The technology also has the potential to solve manufacturing and reliability issues with current bridgewire technology that tends to be fragile in harsh environments.

Perhaps the most appealing aspect of laser ignition is its ability to provide immunity from HERO effects in the modern battlefield. This is certainly a concern with munitions aboard Naval ships employing high-power radar. This is also a problem that concerns fire-suppression and pilot-ejector systems aboard military aircraft. In the end, the path forward for laser ignition relies on finding the right application, engineers with imagination, and those willing to invest in the technology. ■

REFERENCES

[1] Redington, S., C. Macrae, G. Burke, and J. Hirlinger. "Disposable, Miniature Internal Optical Ignition Source for Ammunition Application." U.S. Patent 9,618,307, 11 April 2017.

[2] Redington, S., G. Burke, and J. Hirlinger. "Disposable, Miniature Internal Optical Ignition Source." U.S. Patent 10,415,942, 17 September 2019.

BIOGRAPHIES

STEPHEN REDINGTON, PE, is a senior engineer at DEVCOM-AC, with over 30 years of experience in leading-edge hardware design and development for the military, aerospace, and telecommunications industries. His engineering experience ranges from design conception to product manufacturing in military and private sectors. He has made several innovative advancements in inertial guidance, Global Positioning System, and telecommunications technologies. He holds multiple patents regarding laser ignition and explosives safety, including a patent on vertical soldering for three-dimensional circuit assembly. Mr. Redington holds a B.S. in engineering from Rochester Institute of Technology and a graduate certificate in object-oriented design from New Jersey Institute of Technology.

GREGORY BURKE is a recognized subject matter expert at DEVCOM-AC in high-power laser systems for directed energy, ignition of energetics, and biomedical technologies. He has supported the laser ignition program for the U.S. Army's LW-155 howitzer program as well as the Crusader program. He served as president and principal investigator for Aurora Optics, Inc., where he worked on several contracts with the U.S. Army, Navy, and National Institutes of Health. He holds multiple patents in laser technology, microwave-based medical diagnostics, and other applications merging optics, electronics, and mechanical systems. Mr. Burke holds a B.S. in environmental engineering from Ramapo College.

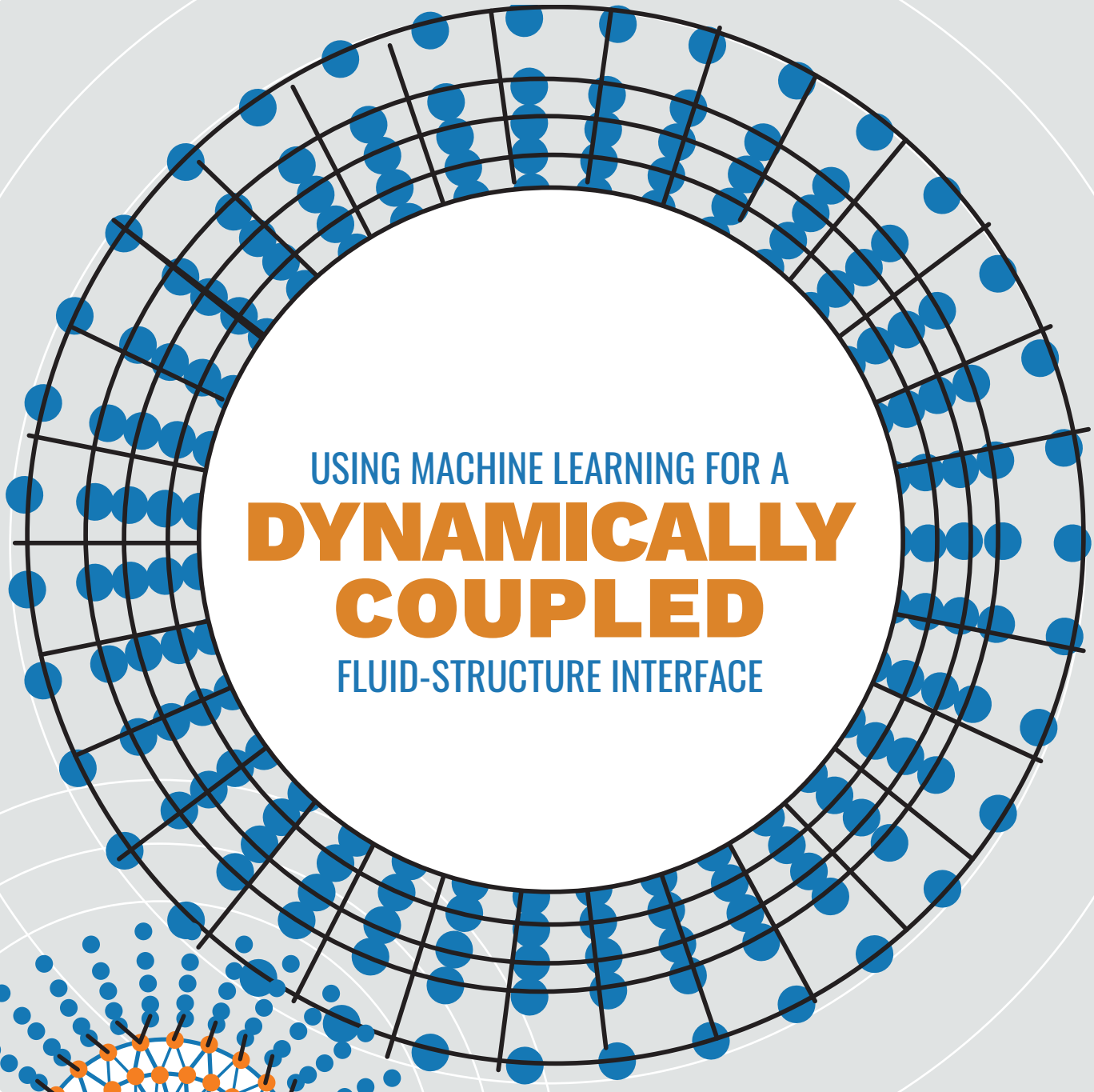

USING MACHINE LEARNING FOR A DYNAMICALLY COUPLED FLUID-STRUCTURE INTERFACE

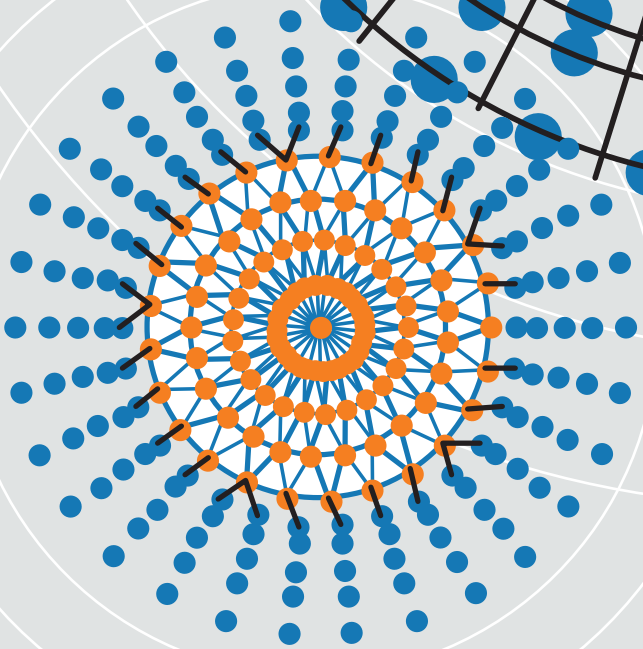

BY RAGINI ACHARYA

(PHOTO SOURCE: R. ACHARYA)

SUMMARY

A dynamically coupled interface has been developed to determine the three-dimensional transient thermo-structural response of the hypersonic vehicle during its flight. Dynamic coupling is required when the change in aerothermal state, surface temperature, ablation, mass/momentum/energy transfer at the surface, and shape change of a hypersonic vehicle due to the thermal loading from the aerothermal environment couples with the structural solver. This results in a strong coupling between the two codes. The coupled codes are more accurate in modelling the interdisciplinary thermo-physico-chemical interactions compared to each separately simulated process. The dynamic coupling is achieved by a code-independent robust and agile python interface that utilizes a tree-based search algorithm to enable nonmatching mesh on the computational domains on the fluid and structural sides. This occurs when the mesh size and node position of the two domains are different and dynamically evolving due to displacement- and/or ablation-induced surface regression. The algorithm performs search associations to find the mesh nodes from both domains at the interface and data interpolations between nonmatching meshes for the quantities to map via the interpolation algorithm.

> ***The dynamic coupling is achieved by a code-independent robust and agile python interface that utilizes a tree-based search algorithm to enable nonmatching mesh on the computational domains on the fluid and structural sides.***

If there is no structural deformation that could affect the calculated flow, the next timestep will be run on the same structural mesh as earlier without any changes. This will allow the program to save time by not having to unnecessarily modify the mesh. In either case, the total grid count in the fluid or solid computational domains will not alter—only the grid will be adapted based upon structural deformations due to mass loss and/or thermo-structural response of the solid. A proof-of-concept of the interface has been developed in-house, and canonical results are shown.

INTRODUCTION

During flight, the hypersonic vehicle is subjected to aerodynamic thermal and mechanical loads transferred to its structure, including the vehicle's thermal protection system. The combined thermal and mechanical loading results in increased surface temperatures, ablation, and mass/momentum/energy transfer at the surface of the hypersonic vehicle. There are two possibilities for the interface between the fluid and the vehicle's outer mold line: (1) surface regression (due to ablation, weather erosion, and/or spallation) and (2) surface deformation (due to the aerodynamic forces exerted on the surface). Both phenomena affect the interface between the fluid and structural domains. To enable coupled, high-fidelity computational simulations of integrated aerothermal-material-structural response of the thermal-protection material (TPS) material when subjected to aerothermal heating, material ablation, and resulting shape change process, it is important to exchange information from both sides. Therefore, the grid deformation of the interface (which is a boundary for the fluid domain) must be determined.

This work aims at enabling high-fidelity simulation of integrated aerothermal-material-structural response of the TPS material when subjected to aerothermal heating, material ablation, and resulting shape change process. To achieve such close coupling, a modular and flexible interface was developed that can dynamically couple a three-dimensional (3-D), transient, aerothermal code with ablation and finite-element analysis codes. Dynamic coupling means that the change in aerothermal state, surface temperature,

ablation, mass/momentum/energy transfer at the surface, and shape change of a hypersonic vehicle couple with the structural solver. This results in a strong coupling between the two codes. The coupled codes are more accurate in modelling the interdisciplinary thermo-physico-chemical interactions associated with an aerothermal flow, 3-D, transient, thermo-structural response of the TPS material while it undergoes shape change.

The dynamic data exchange interface presented in this article is code agnostic. It is developed as a modular stand-alone capability that can be used to perform data exchange between any CFD and structural codes without restrictions on whether they are structured or unstructured. A unique and innovative aspect of this code is its ability to maintain connectivity when the solid shape is changing because of ablation and structural deformation. The flexible interface can enable computational affordability for the coupled, high-fidelity simulations, as it will free the codes from the restriction of having a perfect match at the aerothermal-structural interface in the presence of shape change due to ablation and deformation. Therefore, the computationally affordable, dynamically coupled modelling and simulation capability will deliver an improved methodology for TPS design for hypersonic flight systems.

OBJECTIVES

The purpose of this research was to enable computational simulations of fully coupled fluid-structure phenomena by executing the following objectives:

- Develop the tree-based machine learning (ML) method for data exchange between structured and unstructured mesh, representing typical fluid and structural dynamics solvers, respectively.
- Conduct a demonstration to maintain the interface connectivity under multiple scenarios, including deformation and regression of the interface between the two mesh (i.e., structured and unstructured).

TECHNICAL APPROACH

A partitioned approach has been proposed in which the fluid and structure equations of motion are solved in separate domain-specific solvers and the coupling is provided by an interface. This helps to exchange information between the two solvers via relevant physical variables and mass/momentum/energy conservation at the physical interface of the two solvers (shown in Figure 1). The advantage of this approach is that available solvers for these two separate domains, which have been verified and validated in their specific problem domains, can be used. While the concept appears quite

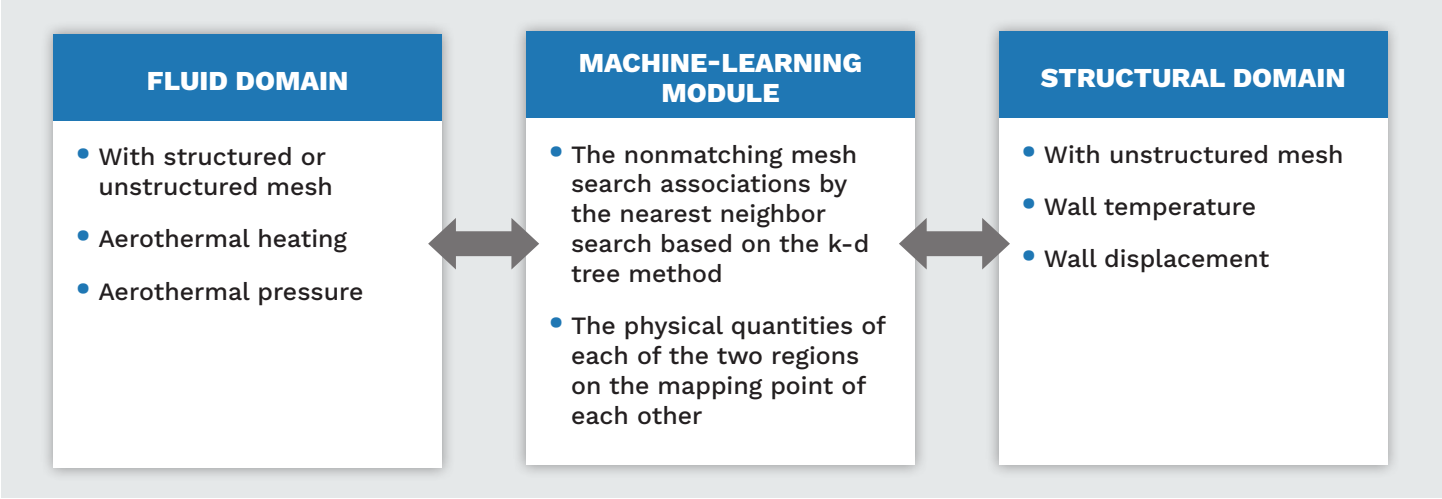

Figure 1. Details of the Interface Methodology *(Source: R. Acharya)*.

straightforward and simple, there are two major research questions: (1) how to update mesh in each computational domain when there is change in interface and (2) how to determine connectivity for information exchange between structured and unstructured mesh. Both research questions can be addressed by the overall workflow shown in Figure 1.

Starting with the structured grid and once converged with the stipulated timesteps, the required data for the unstructured grid solver is communicated via the interface and by utilizing the k-d tree nearest neighbor (NN) search algorithm. This method utilizes matrices to approximate the node locations on the new mesh.

There are two possibilities for the interface: (1) surface regression (due to processes such as ablation, weather erosion, spallation, etc.) and (2) surface deformation (due to the aerodynamic forces exerted on the surface). Each of these affects the interface between the fluid and structural domains; therefore, the grid deformation of the fluid-structure interface must be determined. If there is no structural deformation that could affect the flow, then the next timestep will be run on the same mesh. This will allow the program to save time by not having to unnecessarily convert the mesh file. In either case, the total grid count in the fluid or solid computational domains will not alter—only the grid will be adapted based upon structural deformations due to mass loss and/or thermo-structural response of the solid. This workflow is shown in Figure 2.

k-d TREE SEARCH ALGORITHM

A structured (corresponding to the fluid solver) mesh and an unstructured (corresponding to the structural solver) mesh are likely to have nonmatching points at the interface between the fluid and structural domains. Therefore, an NN search algorithm is implemented to find the respective mesh points for information exchange. An NN search, a form of a proximity search, is the optimization

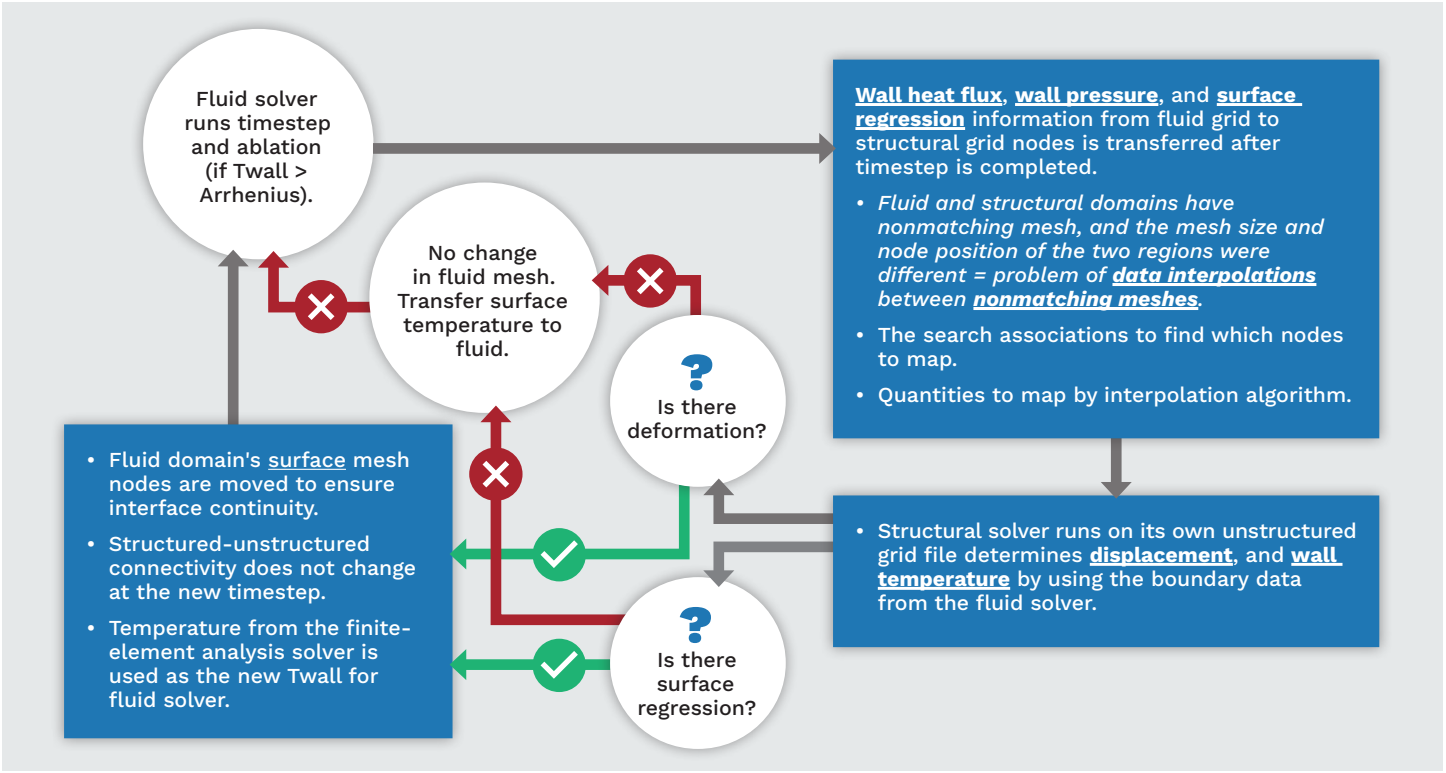

Figure 2. Decision Tree for Mesh Updates in the Fluid Domain *(Source: R. Acharya)*.

problem of finding the point in each set closest (or most similar) to a given point. Mathematically, the NN search problem is defined as follows: given a set S of points in a space M and a query point q ∈ M, find the closest point in S to q. M is represented as the d-dimensional vector space where dissimilarity is measured using a distance. Although the distance can be any metric measure, a standard Euclidean distance is used in this work.

Neighbors-based methods are known as nongeneralizing ML methods since they simply "remember" all data transformed into a fast-indexing structure like a k-d tree. A direct generalization of this problem is a k-NN search, where k closest points are found. Despite its simplicity, the NN technique has been successful in many classification and regression problems. Being a nonparametric method, it is often successful in classification situations where the decision boundary is very irregular.

> ***Neighbors-based methods are known as nongeneralizing ML methods since they simply "remember" all data transformed into a fast-indexing structure like a k-d tree.***

Figure 3 shows a schematic description of a k-d tree method.

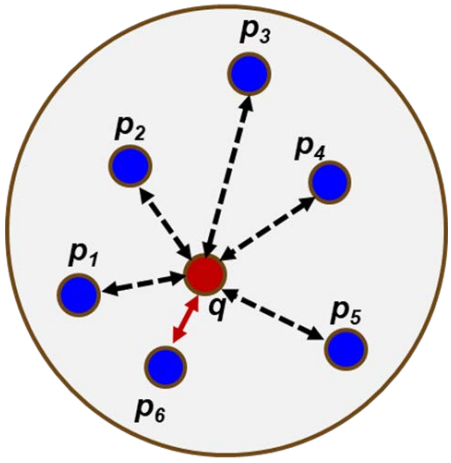

Figure 3. Schematic Description of a k-d Tree Method *(Source: R. Acharya)*.

As shown in the figure, a search is performed to find the NN of point q. There are multiple points in the neighborhood of point q from p_1 to p_6. Standard Euclidean distance from point q to each p_i is calculated, and the point at minimum distance from point q is selected as the NN. In this work, this technique has been expanded to include a two-way search in a two-dimensional (2-D) space, as the fluid-structure interface is a 2-D surface.

RESULTS AND DISCUSSION

The first demonstration of this approach is shown in Figure 4, where the fluid domain is on the left side and structural or solid side is on the right side of the interface between the two domains. The X's represent structured grid nodes, whereas the green dots represent unstructured grid nodes. The red lines connect the nodes on the fluid and solid structure nodes closest to the interface and determine node pairs for data exchange.

Figure 4a shows the section of the interface with five nodes on the fluid and solid sides with 1:1 correspondence. Figures 4b–c show that when the solid nodes move due to expansion, the algorithm still finds the nearest fluid nodes and maintains connectivity for data exchange. Figures 4d–i show that when more nodes are added on either fluid or solid sides, the algorithm still finds the NNs. However, there are equal number of nodes from both fluid and solid sides in these cases. Figure 5 shows how the algorithm connects the nodes of the nonmatching meshes. When nodes are constant but the unstructured nodes move due to expansion, the algorithm still finds the nearest structured nodes. This represents the fluid domain. As with the earlier case, there is 1:1 correspondence between fluid and solid nodes.

Figure 6 shows how the algorithm connects the nodes of the nonmatching meshes. The circle represents a cross section of a circular cylinder subjected to shock heating due to supersonic crossflow. The blue dots represent fluid-structured grid nodes. Even though many flow solvers are unstructured solvers near the surface, it is customary to use a quadrilateral

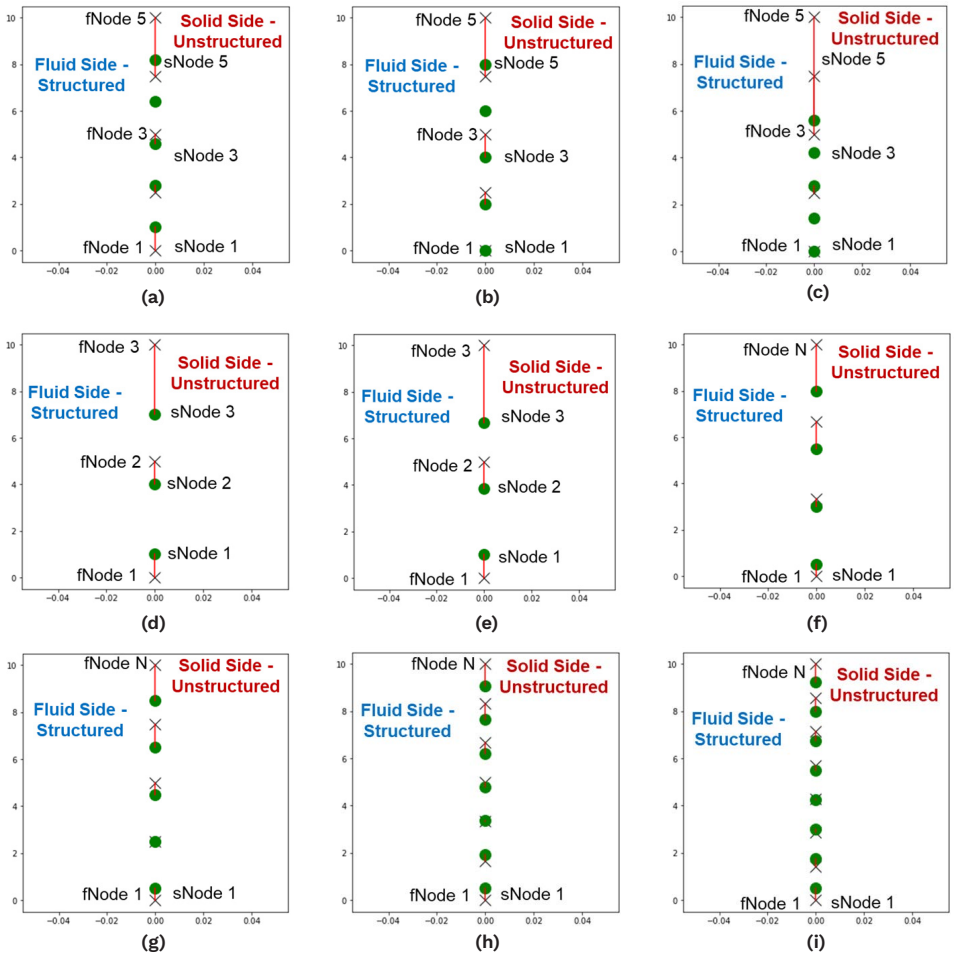

Figure 4. Determining Node Pairs for Data Exchange at the Fluid-Solid Interface *(Source: R. Acharya).*

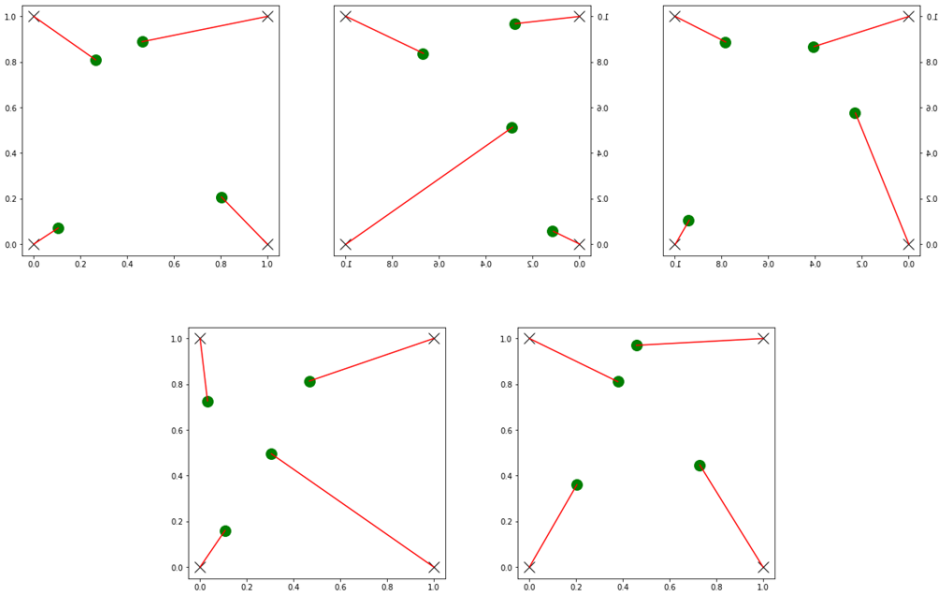

Figure 5. Demonstration of Dynamic Interface for a Surface Mesh Interface *(Source: R. Acharya).*

mesh to resolve the boundary layer. The orange dots represent solid, unstructured grid nodes. The black lines connect the nodes on the fluid and structure nodes closest to the interface. The cross section of the cylinder is replicated in the python interface.

In Figure 6a, the nodes at the interface between fluid and solid sides have 1:1 correspondence. However, in Figure 6b, the node count from the solid side is significantly lower than the fluid side node count at the fluid-structure interface. The k-d-tree-based data exchange code can find the information exchange nodes in both cases. This is trivial when the fluid and structural side mesh match at the interface; but it is encouraging to note that the algorithm is also successful when different mesh densities on the fluid and solid sides are used (as shown in Figure 6b). Such a capability is possible even if the solid side mesh count is significantly less than the fluid side mesh count on the interface, as shown in Figures 7a–d, or when the mesh count on the fluid side of the interface varies, as shown in Figure 8.

These results demonstrate that the dynamic interface code enables the following:

- Both fluid and structure mesh do not need to match at the interface—they can be arbitrary.
- A robust dynamic interface is significantly greater than simple

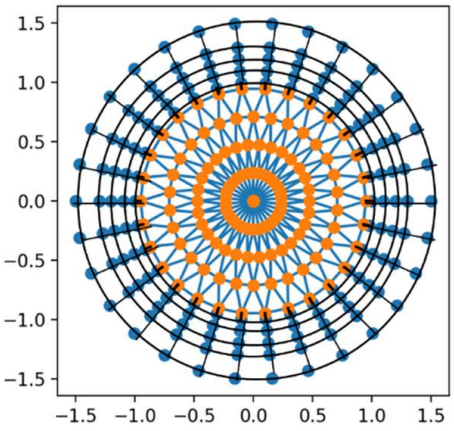

Matched Nodes at the Interface of Fluid and Structural Domains

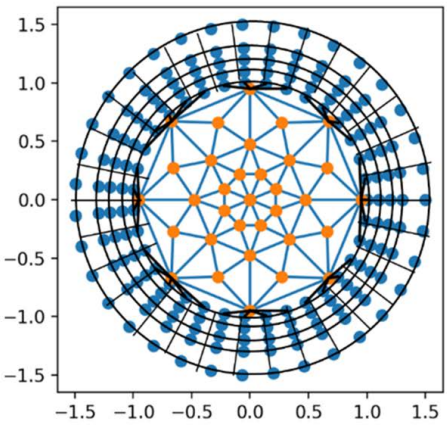

Less Nodes from the Structural Domain vs. the Fluid Domain at Their Interface

Figure 6. Dynamic Interface Identifying Matching Nodes at the Interface for Data Exchange Between Structured and Unstructured Mesh *(Source: R. Acharya)*.

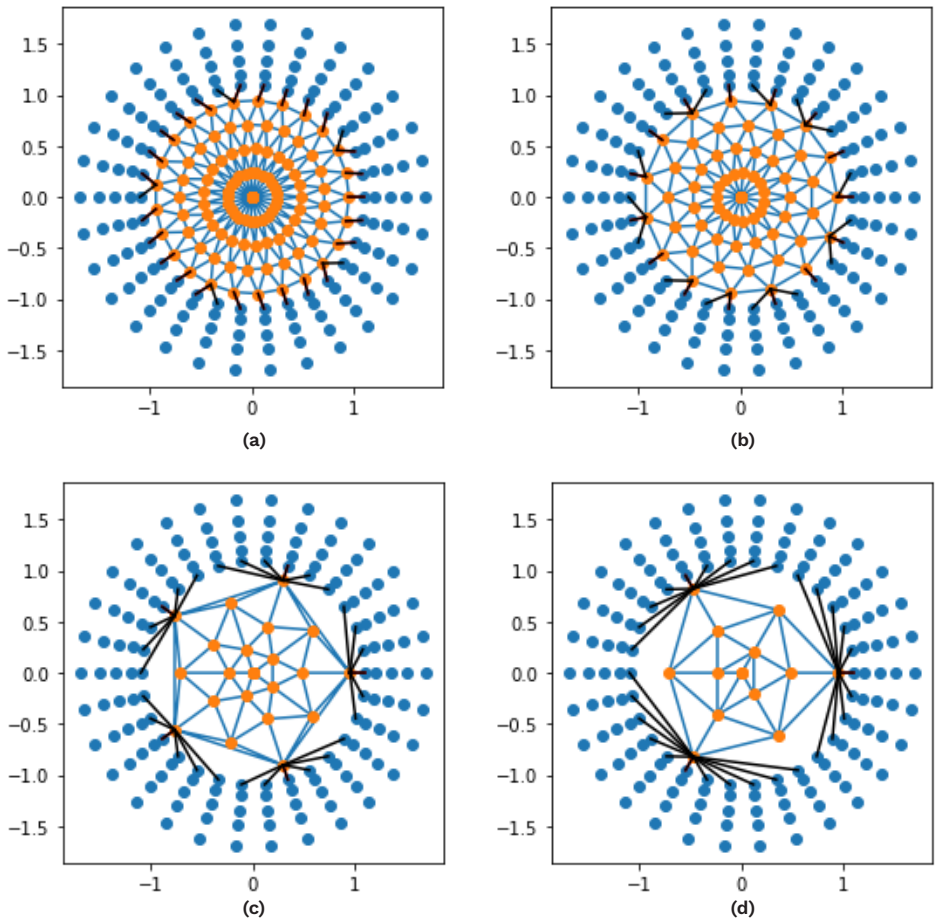

Figure 7. Dynamic Interface Identifying Matching Nodes at the Interface for Data Exchange Between Structured and Unstructured Mesh With Different Mesh Count on the Solid Side *(Source: R. Acharya)*.

mesh overlay with respect to computational cost and accuracy.

The dynamic interface data exchange code is tested when the cylinder deforms from a circular cross section to an elliptical shape. Due to such deformation, the nodes on the solid domain move at the interface (the mesh count remains constant), and the fluid mesh moves accordingly, as shown in Figure 9. The deformation of the cylinder does not affect the connectivity between the fluid and solid mesh at the interface between the two domains. Deformation of cylinder does not affect the fluid-structure node connectivity for the case when the number of mesh count remains constant. However, it is not a constraint for this methodology, as shown in Figure 10.

The dynamic interface data exchange code is then tested when the cylinder ablates and deforms from a circular cross section to an elliptical shape. Due to this ablation, the number of mesh nodes from the structural domain at the fluid-structure interface reduces, while deformation causes the nodes to move from their original locations. The fluid mesh is reorganized to occupy the newly generated fluid volume due to the combined ablation deformation process, as shown in Figure 10. Despite the combined ablation and deformation, the algorithm successfully identifies the nodes in

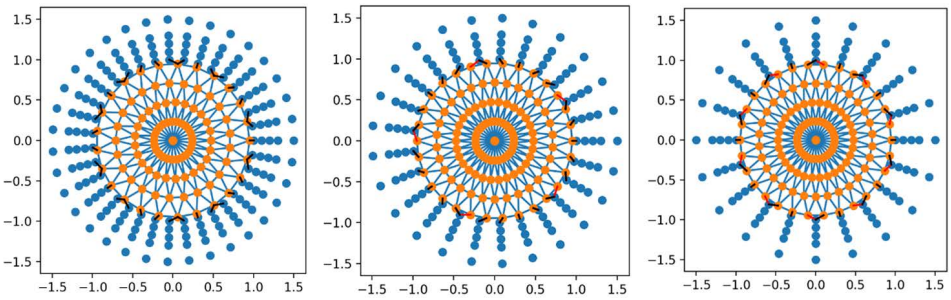

Figure 8. Dynamic Interface Identifying Matching Nodes at the Interface for Data Exchange Between Structured and Unstructured Mesh With Different Mesh Count on the Fluid Side *(Source: R. Acharya)*.

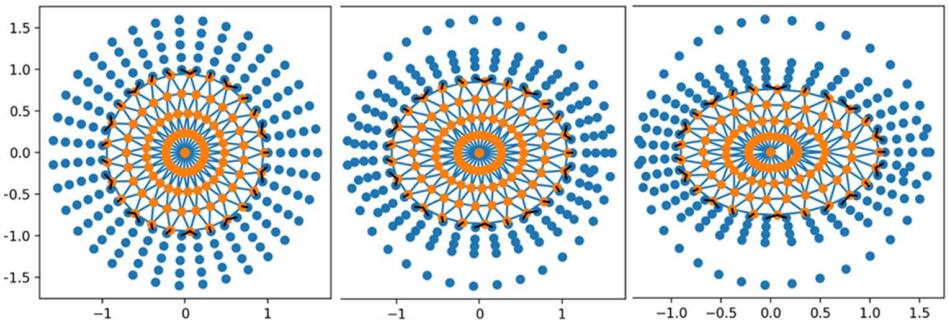

Figure 9. Dynamic Identification of Matching Nodes at the Fluid and Structure Interface When the Cylinder Deforms *(Source: R. Acharya)*.

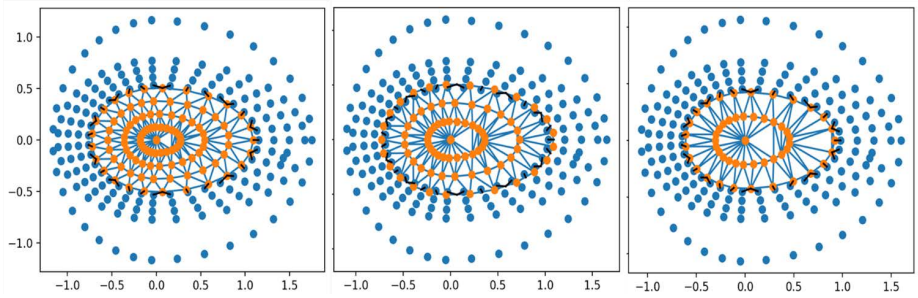

Figure 10. Dynamic Identification of Matching Nodes at the Fluid and Solid Interface When the Cylinder Ablates and Deforms *(Source: R. Acharya)*.

fluid and structural domains where data exchange must occur. Such connectivity is maintained between the fluid and structural mesh at the interface between the two domains. Surface regression of the cylinder requires change in the fluid-structure interface connectivity as the mesh count on the interface from the solid side changes. Two-way connectivity can be readily determined with the capability presented in this work, as shown in Figure 10.

Surface regression of the cylinder requires change in the fluid-structure interface connectivity as the mesh count on the interface from the solid side changes.

In these results, the cylinder's ablation and deformation are shown to be symmetrical around the streamwise direction—this is not a condition of the algorithm but rather a simplification made for demonstration purposes.

CONCLUSIONS

Results from the dynamically coupled interface utilizing a tree-based algorithm show how displacement- and/or ablation-induced surface regression can enable nonmatching mesh on the computational domains on the fluid and structural sides when the mesh size and node position of the two domains are different and dynamically evolving. The tree-based search algorithm performs associations to find the mesh nodes from both domains at the interface and data interpolations between nonmatching meshes for the quantities to map via the interpolation algorithm. This capability can be utilized to determine

the 3-D, transient, thermo-structural response of the hypersonic vehicle during its flight. The dynamically coupled codes can provide higher fidelity results in modelling the interdisciplinary thermo-physico-chemical interactions compared to each separately simulated process, and their effects can translate to the other offline code. ■

BIOGRAPHY

RAGINI ACHARYA is an associate professor in the Mechanical, Aerospace, and Biomedical Engineering Department at the University of Tennessee Space Institute. With over a decade of experience in the aerospace and defense industry, she has been the principal investigator/coinvestigator on hypersonic and propulsion technologies, reacting flow modelling and computations, and uncertainty quantification method development. She coauthored two best-selling, graduate-level textbooks on turbulent and mulitphase combustion; wrote over 50 technical articles in peer-reviewed publications and technical conferences; and received numerous awards. She is an American Institute of Aeronautics and Astronautics (AIAA) Associate Fellow, a member of the Advisory Board National Space and Missile Materials Symposium, and chair of the AIAA High-Speed Air Breathing Propulsion Technical Committee. Dr. Ragini Acharya holds a Ph.D. in mechanical engineering from The Pennsylvania State University.

UASs IN THE MODERN ELECTRONIC BATTLEFIELD

BY HARRY R. LUZETSKY (PHOTO SOURCE: DIGITAL ART RENDERING [123RF.COM])

INTRODUCTION

With dominance of the electromagnetic (EM) spectrum increasing in importance and U.S. military vehicles and systems being faced with an array of threats from various adversaries, control and management of the EM spectrum will determine where future battles are won or lost. Simultaneously, the use of unmanned aerial systems (UASs) in the battlefield for surveillance, targeting, and weapons delivery continues to rise.

The UAS is an aerial electronics platform that can fly without a pilot physically located in the aircraft. It consists of an airframe and a computer system that combines sensors, Global Positioning Systems, servos, central processing units, and sometimes a weapon delivery system. With a configuration like that illustrated in Figure 1, all the elements combine to yield a platform without any direct human intervention that can operate in an autonomous manner controlled from the ground. UAS size, type, and configuration vary depending on the application. These can be large vehicles which rival the size of small, manned vehicles and small enough to be launched by hand or via a portable launch tube.

Considering the heavy reliance on electrical and electronic systems for operation being critical to UAS platforms' success in and control of the modern battlefield, EM hardening of the electronic/electrical systems and protection from external EM events/threats are paramount. Without protection, UAS vehicles can easily be lost, endangering personnel relying on them for information and/or direct battlefield support through armament delivery. Loss can occur through disruption of the communication link as well as through an upset of electrical and electronic systems critical to vehicle operation. Although circuit architecture can be used to mitigate some of the effects, these techniques can be costly, adversely impact system weight, and may be unable to address all aspects of the EM spectrum. Therefore, additional techniques are required to provide protection to operate successfully in the modern battlefield, especially considering the ever-increasing energy levels associated with modern battlefield threats that can generate electromagnetic pulses (EMPs) and high-power microwaves (HPMs).

EM THREATS

The EM spectrum can be challenging for electronics and electrical systems.

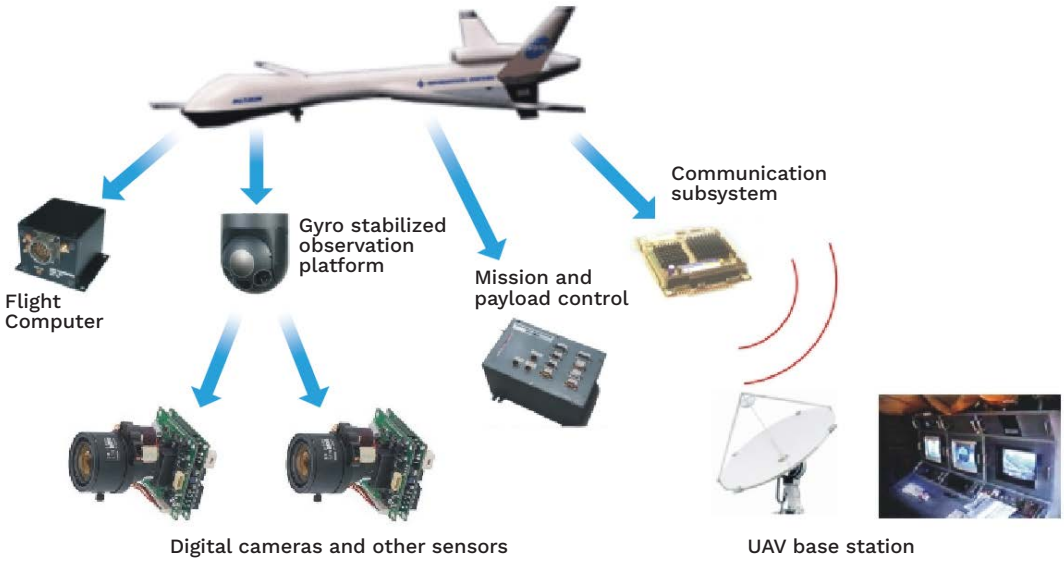

Figure 1. Representative UAS Configuration *(Source: Pastor et al. [1])*.

EM effects can cause upsets and hard failures of electronics and produce power surges that can damage electrical and communication networks. Elements of the EM spectrum provided in Table 1, where an EMP is a major player, identify the threats that comprise the spectrum and possible sources of EM radiation.

Furthermore, the EM threats identified in Table 1 are frequency dependent and require differing shielding levels, as identified in Table 2.

There are two main paths taken by EM radiation to couple with electronics and electrical systems—front and back door coupling. Front door coupling refers to entrances along the ports and openings designed for transmitting EM energy either conducted directly or radiated to communicate with the outer environment. These ports and openings include antennas and sensors designed to communicate with the exterior environment.

Back door coupling refers to those EM entrances not intended for communication with the exterior environment. These entrances include perforations and penetrations associated with cable and mechanical pass-throughs required in designing the UAS. When considering the paths for EM radiation coupling with electronics and electrical systems, entrances can be physical (hole, penetrations, cable runs, etc.) as well as solid (side walls with no EM mitigation properties).

EM THREAT PROTECTION

Protection of electronics and electrical systems typically uses a layered approach (as illustrated in Figure 2), consisting of isolation, EM shielding and filtering, surge protection, and grounding [2]. Of these layers, EM shielding is the most effective for a UAS. Isolation is impractical while filtering; surge protection and grounding are the last lines of defense—coming into play

Table 1. EM Spectrum *(Source: H. R. Luzetsky)*

THREAT	NATURAL	CIVILIAN	MILITARY
Electromagnetic interference/ electromagnetic compatibility (EMI/EMC)	• Lightning • Electrostatic discharge (ESD) • Solar flares • Auroras	• Communication (cell towers) • Generators • Power supplies • High-voltage electrical transmission lines	• Jammers • Installed electrical equipment • Radios
EMP	• Lightning electromagnetic pulse • ESD • Meteoric EMP • Coronal mass ejection	• Electric circuity switching • Electric motors • Gasoline ignition systems • Continual switching of digital electric • Power line surges	• Nuclear EMP • Nonnuclear EMP • High-altitude EMP (HEMP)
HPM	• Supernova	• High-power radars with relativistic klystron amplifier	• Backward wave oscillator, directed energy weapon

Table 2. Frequency and Shielding Ranges for EM Threats *(Source H. R. Luzetsky)*

THREAT TYPE	FREQUENCY RANGE	EM SHIELDING RANGE
EMI/EMC	9 kHz–40 GHz	60–100 dB
EMP	100 MHz–100 GHz	80–120 dB
HPM	1 GHz–35 GHz	100–140 dB

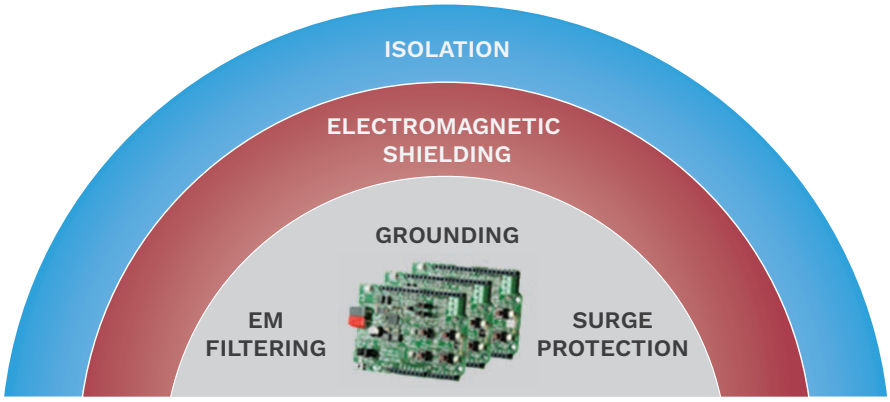

Figure 2. EM Protection Layering for Electronics and Electrical Systems *(Source: H. R. Luzetsky)*.

once energy from an EMP penetrates outer protection layers, impacting the electrical and electronic components. With appropriate EM shielding, the EMP can be stopped or significantly reduced before reaching the electrical and electronic components. Any remaining EM threats can then be easily addressed by filtering, surge protection, and grounding.

For UAS platforms, providing protection to safeguard electrical/electronic systems against these threats for reasonable weight can be a challenge since the UAS structure is a simple, lightweight, aerodynamically efficient, and stable platform with limited space for avionics and payloads. To address the hardening of UAS platforms to the growing EM modern battlefield, assessments of UAS platforms against current and future EM environments have been gaining impetus and importance. Assessments have shown that current UAS platforms do not possess the EM protection needed to circumvent damage or potential loss from high-energy EMP events, and their electronic systems are vulnerable to disruption, upset, and even destruction. With vulnerabilities defined, efforts are ongoing to develop solutions that target those vulnerabilities, reducing them and improving vehicle survivability.

In addition, due to the operational characteristics of UAS platforms, there is a need to transmit and receive across specific frequencies and remain open to support the various operations. This translates to a need to create either transient or permanent frequency windows of transparency within the platform. Creating a shielded structure around the electronics and electrical systems of a UAS platform provides an overall level of EMP protection for the enclosed systems. Systems like sensors and antennas would be mounted to the exterior of the protected area to support unrestricted transmission and receipt of information necessary for the UAS platform operation. External equipment connected to internally protected systems through shielded cables represents a pathway for EMP radiation to reach the internal systems and must then rely on EM filtering and surge protection to defeat the threat.

The key aspect to providing EM threat protection is enclosing a critical electrical and electronic system within an EM shielded structure to provide a baseline level of protection and then handling the penetrations like cabling with other techniques such as EM filtering and surge protection. The difficultly for UAS platforms is that traditional methods of protection to achieve levels defined in Table 2 are thick metal enclosures like 0.125-in-thick aluminum, which tends to be a parasitic weight not tolerated by a UAS platform because of the impact to its operational capability. Efforts have been and are still ongoing to develop composite and polymeric materials with integrated EM shielding. These types of materials provide a means to integrate EM into a UAS platform without incurring significant weight growth to the system.

The key aspect to providing EM threat protection is enclosing a critical electrical and electronic system within an EM shielded structure to provide a baseline level of protection.

MATERIAL WITH INTEGRATED EM SHIELDING

Numerous efforts exist to develop lightweight EM shielding solutions for aircraft structures, with a focus on electronic enclosure boxes. A review of existing techniques has been conducted through a Defense Systems Information Analysis Center report (Figure 3), which highlights EM protection levels afforded by current metal and composite materials [3]. Levels achievable with current materials were observed to be significantly less than that required to protect against threats identified in Table 2.

Developmental efforts to enhance EM capability have been largely centered on additives to formable thermoplastics to enhance EM shielding and electronic approaches like EM filters and active surge protectors. These efforts continue to fall short of the protection requirements identified in Table 2. In addition, application of these solutions still tends to add parasitic weight to the vehicle. For UAS platforms with no room for weight growth, this often results in omission of any EM protection, which can be devastating in the modern commercial and battlefield environment.

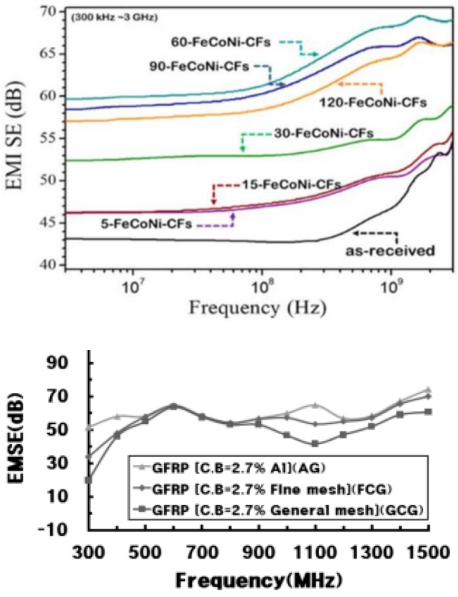

Figure 3. EM Shielding Effectiveness of Different Materials *(Source: Piner et al. [3])*.

Reconciliation of weight with required EM shielding involves developing a multifunctional material that provides structural properties suitable for constructing a UAS while providing EM shielding capable of meeting the shielding requirements specified in Table 2. A recently developed, multifunctional, composite material form originally made for an electronic enclosure box provides a way to achieve high levels of EM shielding with minimal, if any, weight impact to an aircraft structure, particularly for a UAS.

MULTIFUNCTIONAL COMPOSITE MATERIAL DEVELOPMENT

A multifunctional composite material with integrated EM shielding suitable for application to a UAS structure was initially developed under a U.S. Air Force (AF) Small Business Innovation Research (SBIR) program AF 131-110, titled "Electromagnetic Hardened Composite Enclosures for Aircraft Systems" [4]. The material was developed from a graphite-reinforced composite in which expanded copper mesh was integrated using a specially designed in situ tape placement head. In the manufacturing process, the raw material is heated using a laser heat source and consolidated/compacted with a rigid steel roller. The process, illustrated in Figure 4, relies on the combination of localized heat and pressure from the compaction roller to consolidate the laminate. This process is critical to achieving intimate contact between the graphite fibers and copper mesh to reach the levels of conductivity necessary to support high levels of EM shielding.

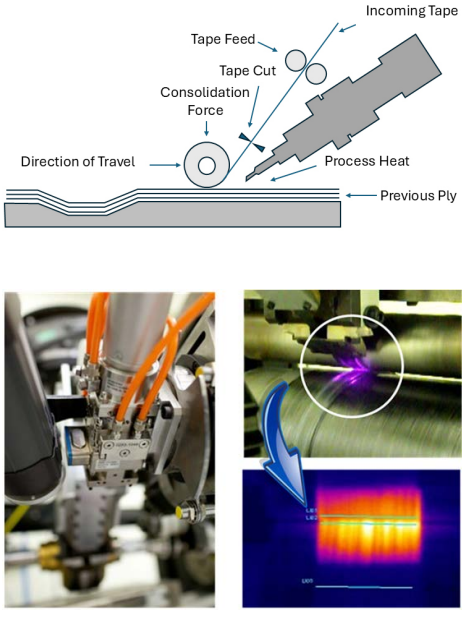

Figure 4. In Situ Automated Fiber Placement (AFP) Process With Laser Heat Source *(Source: TSS/Albany)*.

In the original AF SBIR AF131-110, an electronic enclosure was created at ~25% the weight of a representative metallic enclosure (~1/8-in-thick aluminum), demonstrating an EM shielding effectiveness equivalency. The measured shielding effectiveness of the developed material was approximately between 90 and 135 dB, depending on frequency. Below 1 MHz, measured values were between 120 and 135 dB; from 1 to 10 MHz, measured values were between 135 and 90 dB; from 10 MHz to 10 GHz, values were between 90 and 110 dB; and over 10 GHZ, values were between 110 and 120 dB. Current EM-shielded, nonmetallic enclosures exhibit EM shielding effectiveness levels between 30 and 70 dB, depending on frequency (Figure 3), which is significantly less than that exhibited by the developed material under AF131-110.

From this initial development, material properties were examined. The impact to mechanical properties was minimal. In combination with the in situ tape placement, the material was adaptable to an aircraft structure. Efforts moved forward to demonstrate the capability for providing structural and EM shielding properties suitable for a UAS.

Recently completed, developmental research with a multifunctional composite material has provided a technique and approach for expanding the shielding levels of a UAS fuselage to levels equal to metallic construction at a fraction of the weight. This enhances their capability in the modern EM battlefield. In addition, the additive manufacturing process creates the potential to increase these levels even further with discrete placement and quantity of select materials and their forms into the base laminate. Due to the multifunctional aspects for the developed material form and the manufacturing integration process, custom-designed structures can be developed. This is demonstrated with a representative UAS fuselage with shielding integrated into those areas protecting the electronics and electrical systems.

The developed, multifunctional composite material consisted of an intermediate modulus graphite fiber (IM7)/polyetheretherketone composite with integrated, expanded copper mesh discretely placed within the composite laminate. This is shown in a cross section of the material in Figure 5. Through evaluating various laminate configurations, it was determined that the number and location of mesh layers within the laminate impact the EM shielding and mechanical property characteristics.

Developmental research with a multifunctional composite material has provided a technique and approach for expanding the shielding levels of a UAS fuselage to levels equal to metallic construction at a fraction of the weight.

Computerized tomography (CT) scans were used to evaluate the condition of the as-processed copper mesh in the laminate, including distortion, overlaps, and variation of mesh openings from processing. Multiple CT scans were conducted with a voxel size of 2.14 μm or 8.4 μm.

Figure 6 shows the CT images that illustrate the general configuration of the as-processed mesh. While the general shape of the copper mesh was retained, it was observed that the

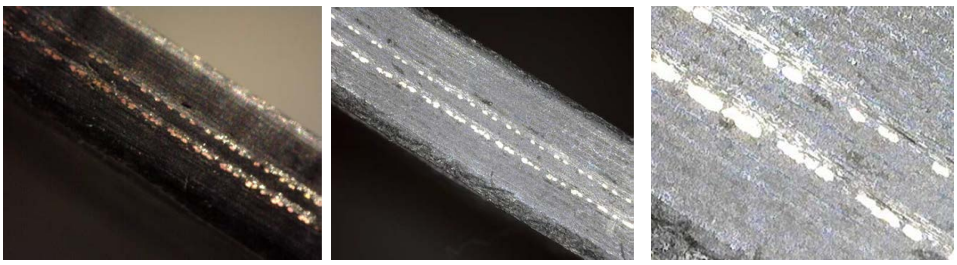

Figure 5. Magnified Cross Sections of Multifunctional Material *(Source: H. R. Luzetsky).*

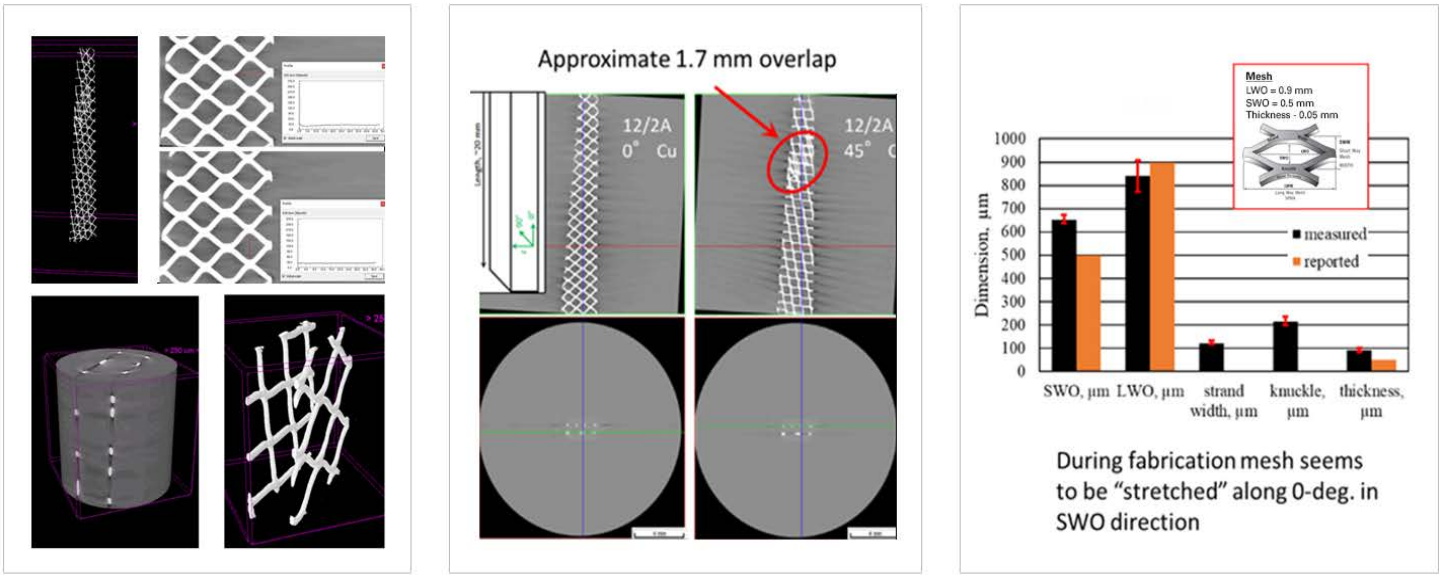

Figure 6. CT Scans Illustrating Copper Mesh Configuration in the Laminate From Processing *(Source: H. R. Luzetsky)*.

fabrication process tended to elongate the mesh along the 0° direction, altering the short-way-of-opening dimension. In addition, there was a slight reduction in the size of the overlap in certain areas; however, the tape overlaps were present, as designed.

Exploration of various laminate configurations, including the percentage of copper mesh and its placement within the laminate, determined ideal configurations to provide the greatest EM shielding with the least impact to mechanical properties. Evaluations were conducted on flat panels and demonstrated potential EM shielding levels between 90 and 100 dB across most frequencies between 9 kHz and 40 GHz, with some frequencies peaking at 110 dB.

MULTIFUNCTIONAL COMPOSITE APPLICATION TO THE UAS PLATFORM

While flat panels are an effective means to screen laminate configurations for their EM shielding capability, there is a geometry component that involves the volume and shape of the structure to which the shielding is being applied. Even with the small volume of most UAS platforms, a multifunctional, EM-shielded composite provides a viable method for reducing the vulnerability of a UAS platform to EM threats. This capability is best evidenced through the developing and EM testing of a representative, small, tube-launched UAS fuselage structure.

A UAS test platform was configured according to the following parameters:

> ***A multifunctional, EM-shielded composite provides a viable method for reducing the vulnerability of a UAS platform to EM threats.***

- The UAS must deploy from a common launch tube, pneumatically integrated launch system, and/or reconfigurable integrated weapons platform.
- Dimensionally, the UAS must fit within a 6–8-in-diameter launch tube.
- The UAS demonstrator must support the integration of foldable wings and strakes.
- Maximum UAS weight, including payload, cannot exceed 30 lb. Included in this payload is a battery-

powered propulsion system and a sensor package (e.g., electrooptical, infrared, synthetic aperture radar, and/or light detection and ranging).

From these basic parameters, the EM composite's structural design and weight criteria were established for the test platform, which is shown in Figure 7. The schematic illustrates the construction of the test platform, which consisted of a fuselage with end enclosures that utilized the multifunctional composite material to create an EM shielded structure. A platform was placed within the formed structure to support a receiving antenna during EM shielding tests.

The EM design parameters of the demonstration structure are listed in Table 3. These design requirements provided a threshold and two objective EM shielding effectiveness levels as a function of frequency.

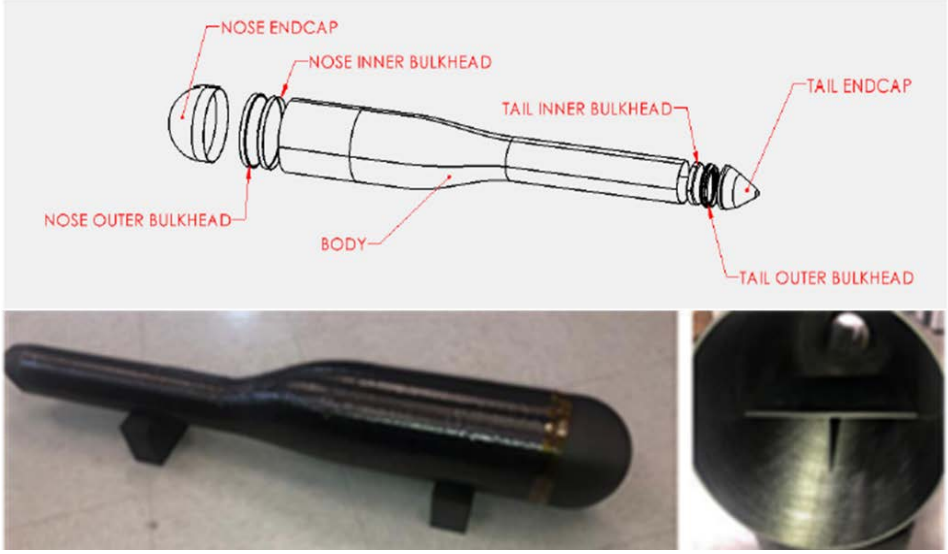

Figure 7. Tube-Launched UAS Test Platform *(Source: H. R. Luzetsky)*.

To explore the potential EM shielding, three laminate configurations were constructed for EM shielding evaluation. These configurations were based on the number of incorporated layers of copper mesh that, while meeting the basic requirements, defined the potential EM shielding effectiveness of the UAS laminate with the multifunctional composite. They included no layers, two layers, and four layers of copper mesh. The laminate configurations were determined from flat panel tests designed to characterize the EM shielding properties as applied to the representative tube launched demonstrator structure. The results of the EM shielding tests are provided in Table 4.

Table 3. EM Shielding Design Parameters for the UAS Demonstrator *(Source: H. R. Luzetsky)*

EM TYPE/THREAT	FREQUENCY RANGE	THRESHOLD	OBJECTIVE 1	OBJECTIVE 2
EMI/EMC	9 kHz–40 GHz	60 dB	80 dB	100 dB
EMP	100 MHz–100 GHz	80 dB	100 dB	120 dB
HPM	1–35 GHz	100 dB	120 dB	140 dB

Table 4. EM Shielding Summary for the UAS Demonstrator *(Source: H. R. Luzetsky)*

EM TYPE/THREAT	FREQUENCY RANGE	MINIMUM	MAXIMUM	AVERAGE
EMI/EMC	9 kHz–40 GHz	60 dB	80 dB	70 dB
EMP	100 MHz–100 GHz	80 dB	100 dB	90 dB
HPM	1–35 GHz	100 dB	120 dB	110 dB

CONCLUSIONS

The application of a multifunctional composite with integrated shielding demonstrated a viable method to enhance the shielding effectiveness of a UAS fuselage structure. A demonstration structure demonstrated threshold reductions in the 50-MHz–18-GHz range of the EM spectrum while not exceeding the weight of the state-of-the-art unshielded fuselage skin. Additional work with this material on a larger fuselage structure demonstrated even higher shielding levels, which are only enhanced further when coupled with internal electronics enclosure structures for internal electrical and electronic modules.

More work is required to explore shielding around perforations in the fuselage structure, such as access panels and installation of sensors and antennas. In addition, variability of the protection level with frequency indicated the potential to customize the EM shielding per frequency. This would provide an opportunity to design windows in the structure to facilitate EM transmission to support sensor and communication transmission at specific frequencies while blocking it at others. ■

REFERENCES

[1] Pastor, E., J. Lopez, and P. Royo. "A Hardware/Software Architecture for UAV Payload and Mission Control." Department of Computer Architecture, Technical University of Catalonia Castelldefels, (Barcelona), Spain, article in *IEEE Aerospace and Electronic Systems Magazine*, July 2007.

[2] U.S. Air Force Civil Engineer Center (AFCEC). "High Altitude Electromagnetic Pulse (HEMP) Effects and Protection." High Altitude Electromagnetic Pulse (HEMP) Effects and Protection | WBDG - Whole Building Design Guide, updated 7 August 2020.

[3] Piner, R., D. Motes, and T. Kneen. "Development of EMI Shielding Capabilities of Fiber Reinforced Composites." DSIAC Technical Inquiry (TI) Response Report, February 2022.

[4] U.S. Department of Defense. "Electromagnetic Hardened Composite Enclosures for Aircraft Systems." AF131-110, SURVICE Engineering Company SBIR, 2013.

BIOGRAPHY

HARRY R. ("RICK") LUZETSKY is a subject matter expert in composites and survivability at SURVICE Engineering Company's Aberdeen Research Organization – Research and Analysis Group. He currently supports the U.S. Army Evaluation Center in the survivability assessment of military platforms and has been involved in developing a ballistic-tolerant composite drive shaft, armored actuators, a thermoplastic tail cone, and a multifunctional composite material with structural and integrated electromagnetic shielding capabilities for military platform structures. He has over 40 years of experience with vertical lift aircraft, specializing in composite materials and survivability technology enhancements to improve platform performance. He holds two autonomous, self-sealing, fuel-bladder patents. Mr. Luzetsky holds a B.S. in materials engineering from Drexel University.

DSIAC JOURNAL

The Defense Systems Information Analysis Center (DSIAC) is a component of the U.S. Department of Defense's (DoD's) Information Analysis Center (IAC) enterprise, serving the defense enterprise of DoD and federal government users and their supporting academia and industry partners.

HTTPS://DSIAC.DTIC.MIL

CONNECT WITH US ON SOCIAL MEDIA